A&A, 678, A137 (2023)
https://doi.org/10.1051/0004-6361/202346491

Astronomy & Astrophysics

CoCCoA: Complex Chemistry in hot Cores with ALMA

Selected oxygen-bearing species

Y. Chen (陈缘)[1], M. L. van Gelder[1], P. Nazari[1], C. L. Brogan[2], E. F. van Dishoeck[1,4], H. Linnartz[5], J. K. Jørgensen[6], T. R. Hunter[2,3], O. H. Wilkins[7], G. A. Blake[8], P. Caselli[4], K.-J. Chuang[5], C. Codella[9,10], I. Cooke[11], M. N. Drozdovskaya[12], R. T. Garrod[13,14], S. Ioppolo[15], M. Jin[16,17], B. M. Kulterer[12], N. F. W. Ligterink[18], A. Lipnicky[2], R. Loomis[2], M. G. Rachid[5], S. Spezzano[4], and B. A. McGuire[2,19]

(Affiliations can be found after the references)

Received 20 March 2023 / Accepted 1 August 2023

ABSTRACT

Context. Complex organic molecules (COMs), especially the oxygen-bearing species, have been observed to be abundant in the gas phase toward low-mass and high-mass protostars. Deep line surveys have been carried out only for a limited number of well-known star-forming regions using the Atacama Large Millimeter/submillimeter Array (ALMA), which has unprecedented resolution and sensitivity, and statistical studies on oxygen-bearing COMs (O-COMs) in a large sample of high-mass protostars using ALMA are still lacking.

Aims. We aim to determine the column density ratios of six O-COMs with respect to methanol (CH_3OH) in a sample of 14 high-mass protostellar sources in order to investigate their origin through ice and/or gas-phase chemistry. The selected species are: acetaldehyde (CH_3CHO), ethanol (C_2H_5OH), dimethyl ether (DME; CH_3OCH_3), methyl formate (MF; CH_3OCHO), glycolaldehyde (GA; CH_2OHCHO), and ethylene glycol (EG; $(CH_2OH)_2$).

Methods. We fit the spectra of 14 high-mass sources observed as part of the Complex Chemistry in hot Cores with ALMA (CoCCoA) survey and derived the column densities and excitation temperatures of the six selected O-COMs. We used the minor isotopologue of methanol $CH_3^{18}OH$ to infer the column density of the main isotopologue CH_3OH, of which the lines are generally optically thick. We compared our O-COM ratios with those of five low-mass protostars studied with ALMA from the available literature as well as with the results from experiments and simulations.

Results. Although the CoCCoA sources have different morphologies and brightness in their continuum and methanol emission, the O-COM ratios with respect to methanol have very similar values in the high-mass and low-mass samples. The DME and MF have the highest and most constant ratios within one order of magnitude, while the other four species have lower ratios and exhibit larger scatter by one to two orders of magnitude. The ratio between DME and MF is close to one, which agrees well with previous observational findings. Current simulations and experiments can reproduce most observational trends with a few exceptions. For example, they tend to overestimate the abundance of ethanol and GA with respect to methanol.

Conclusions. The constant column density ratios of the selected O-COMs among the low- and high-mass sources suggest that these species are formed in similar environments during star formation, probably on icy dust grains in the pre-stellar stages. Where deviations are found, hypotheses exist to explain the differences between observations, simulations, and experiments, such as the involvement of gas-phase chemistry and different emitting areas of molecules.

Key words. astrochemistry – stars: protostars – stars: massive – stars: formation – ISM: abundances – techniques: interferometric

1. Introduction

Complex organic molecules (COMs), typically defined as carbon-bearing molecules with at least six atoms (Herbst & van Dishoeck 2009), have been intensively studied over the past several decades due to their importance of linking atoms and simple molecules with prebiotic species (Caselli & Ceccarelli 2012; Jørgensen et al. 2020; Ceccarelli et al. 2022). Up to now, more than 80 COMs have been detected in various environments (McGuire 2022). Nearly or fully saturated COMs containing oxygen and nitrogen atoms have been widely observed in line surveys of protostars with different masses by radio telescopes (e.g., Belloche et al. 2016, 2020; Jørgensen et al. 2016; El-Abd et al. 2019; Lee et al. 2019a; Csengeri et al. 2019; Bianchi et al. 2020; van Gelder et al. 2020; Ligterink et al. 2020; Mininni et al. 2020; Colzi et al. 2021; Nazari et al. 2021, 2022a; Hsu et al. 2022; Imai et al. 2022; Codella et al. 2022). In particular, oxygen-bearing COMs (O-COMs), including methanol (CH_3OH), acetaldehyde (CH_3CHO), dimethyl ether (DME; CH_3OCH_3), and methyl formate (MF; CH_3OCHO), were first observed in massive star-forming regions more than two decades ago (Cummins et al. 1986; Blake et al. 1987; Schilke et al. 1997). They were also detected in subsequent observations of the low-mass protostars IRAS 16293–2422 (Cazaux et al. 2003) and NGC 1333 IRAS 4A/2A (Bottinelli et al. 2004; Jørgensen et al. 2005). Larger O-COMs, such as glycolaldehyde (GA; CH_2OHCHO) and ethylene glycol (EG; $(CH_2OH)_2$), were first detected in the high-mass star-forming cluster Sgr B2(N) near the Galactic center (Hollis et al. 2000, 2002) and then in other protostellar sources (Beltrán et al. 2009; Maury et al. 2014). Three abundant COMs, CH_3OH, CH_3CN, and DME, were even detected in protoplanetary disks around more evolved young stellar objects (Öberg et al. 2015; Walsh et al. 2016; Brunken et al. 2022).

However, the formation mechanisms of COMs are still under debate. The observed O-COMs were initially thought to exist exclusively in the gas phase in hot ($T \gtrsim 100$ K) environments around protostars (i.e., hot cores and hot corinos), primarily from thermal desorption of ices (Herbst & van Dishoeck 2009; Jørgensen et al. 2020). On the other hand, observations in the past decade started detecting them in cold ($T \sim 10$ K) pre-stellar cores, albeit in low abundances (Bacmann et al. 2012; Vastel et al. 2014; Jiménez-Serra et al. 2016; Soma et al. 2018; Scibelli et al. 2021). These detections indicate that COMs may already be formed on the surfaces of dust grains in the early pre-stellar stages before any ice desorption or subsequent gas-phase chemistry occurs. Simulations and experiments have found that solid-phase methanol can be formed in the ice mantles of dust grains. The formation begins with a series of CO hydrogenation under both energetic (e.g., UV radiation) and non-energetic (e.g., atom addition) conditions (Hiraoka et al. 1998; Shalabiea & Greenberg 1994; Watanabe & Kouchi 2002; Fuchs et al. 2009; Cuppen et al. 2009; Simons et al. 2020). Formation of bigger COMs on cold dust grains is also possible. Experiments by Fedoseev et al. (2015) show that GA and EG can be formed through surface hydrogenation of CO under cold, dense cloud conditions (T = 12 K). A follow-up experimental study by Chuang et al. (2016) mixed CO, H_2CO, and CH_3OH ices at T = 15 K and produced not only GA and EG but also some MF in the solid phase. However, compared with observational results in the gas phase, MF was underproduced in their experiments, while GA and EG were overproduced. The underproduction of MF was alleviated in Chuang et al. (2017) by introducing UV irradiation, which may photodissociate the initial ingredients in the mixed ice into reactive free radicals and therefore boost the formation of larger species. Based on these laboratory works, Simons et al. (2020) explored the dependence of the final grain mantle composition on the initial gas-phase composition and the dust temperature by chemical simulations. Their simulations were still able to produce MF, GA, and EG at temperatures as low as 8 K, but MF was again underestimated (without UV). A much higher abundance of MF has been reproduced by Garrod et al. (2022), who introduced a set of non-diffusive mechanisms to their simulations (see detailed discussions in Sect. 5). These studies show that the abundances of some COMs, such as MF, may depend on environmental conditions, and a debate still exists whether and to what extent gas-phase chemistry is involved in their formation (Balucani et al. 2015; Ceccarelli et al. 2022).

With the development of new observational techniques, it is now possible to make a more complete inventory of COMs in star-forming regions. The Protostellar Interferometric Line Survey (PILS; Jørgensen et al. 2016) using the Atacama Large Millimeter/submillimeter Array (ALMA) detected more than 20 COMs, including all the O-bearing species mentioned above plus ethanol (C_2H_5OH) and some of their isotopologues in the low-mass protostellar binary IRAS 16293–2422 A and B (Jørgensen et al. 2018; Manigand et al. 2020). Recent ALMA surveys of a larger sample of sources have further confirmed the ubiquity of COMs in both low- and high-mass protostars (van Gelder et al. 2020; Yang et al. 2021; Nazari et al. 2022a). The next step in COM studies is therefore to investigate similarities and differences in COM abundances and their ratios among different types of sources in order to constrain their formation routes. Indeed, surveys have revealed an interesting consistency of O-COM ratios with respect to methanol among different sources. Coletta et al. (2020) summarized single-dish observations of DME and MF in various objects, including pre-stellar cores, star-forming regions, a protostellar shock, and galactic center cores. They found that DME and MF abundances are strongly correlated with a ratio of about one. As another example, van Gelder et al. (2020) report constant ratios of O-COMs with respect to methanol in five low-mass protostars. For N-bearing species, Nazari et al. (2022a) also found rather constant ratios with respect to methyl cyanide (CH_3CN) in more than 30 high-mass sources, though some species, such as formamide (NH_2CHO), show a larger scatter in their ratios. The constant abundance ratios revealed by observations are interesting since different objects have different physical environments, which are expected to influence the chemical evolution and alter the ratios among COMs. These similarities suggest that COMs are mainly formed under similar physical conditions, probably on the surfaces of dust grains during the cold pre-stellar phase.

Previous observational studies mostly focused on a small number of well-known sources, and many of them did not have enough spatial resolution and sensitivity to overcome beam dilution and optical depth issues. So far, a few ALMA surveys with enhanced sensitivities and resolutions on O-COMs in low-mass protostellar regions have been published (van Gelder et al. 2020; Hsu et al. 2022), but results for the high-mass counterparts, especially from ALMA surveys that cover minor isotopologues of methanol, are still lacking. We emphasize the importance of detecting optically thin lines of minor isotopologues of methanol, which requires higher sensitivity, in order to better constrain the column density of methanol and hence the ratios with respect to other O-COMs. There are several ALMA studies on O-COMs in the high-mass counterparts (e.g., Csengeri et al. 2019; El-Abd et al. 2019; Mininni et al. 2020), but all of them are case studies that do not use minor isotopologues of methanol in their analyses and/or only focus on a small set of O-COMs, such as the $C_2H_4O_2$ isomers. High-mass protostellar regions are important to the investigation of COM chemistry under different physical conditions, and given the higher temperatures and the possibly enhanced UV radiation along outflow cavity walls, it is expected that the gas-phase data from high-mass sources will give a better representation of the solid-phase abundances, as icy COMs are expected to be mostly thermally desorbed from dust grains. It is also timely to present the results of ALMA observations on high-mass sources after the latest development of a comprehensive model on COM chemistry in hot cores by Garrod et al. (2022).

In this paper, we present the analysis of O-COMs observed in 14 high-mass star-forming regions in the Complex Chemistry in hot Cores with ALMA (CoCCoA) survey. The analysis is focused on six O-bearing COMs, C_2H_5OH, CH_3CHO, DME, MF, GA, and EG (including two conformers, anti and gauche, *a*-EG and *g*-EG), as well as two methanol isotopologues, $^{13}CH_3OH$ and $CH_3^{18}OH$. Covering minor isotopologues of methanol is essential because the lines of the main isotopologue, $^{12}CH_3^{16}OH$, are likely to suffer from a high optical depth, in which case its column density needs to be inferred from optically thin lines of a minor isotopologue. To this sample, we added C_2H_5OH and CH_3CHO for their potential detections in ices (Schutte et al. 1999; Yang et al. 2022; McClure et al. 2023). We selected MF, GA, and EG in order to study their relative abundances, based on laboratory and modeling findings in Chuang et al. (2017) and Simons et al. (2020). Finally, we included DME because of its high abundance observed in star-forming regions.

This work will provide a base for comparison with future observations of icy COMs by the *James Webb* Space Telescope (JWST). To verify if COMs are formed in ices, a direct approach is to observe their vibrational absorption features in

the infrared. However, this requires very high sensitivity and spectral resolution in the fingerprint wavelength range at ~2–15 μm, which has only become feasible with the successful operation of JWST. So far, methanol is the only COM that has confirmed detections in interstellar ices, whereas several other solid-phase COMs, such as C_2H_5OH and CH_3CHO, have only been tentatively identified (see review by Boogert et al. 2015, and references therein). Recently, several JWST teams have started hunting for solid-phase COM features (Yang et al. 2022; McClure et al. 2023). Important laboratory measurements of COM infrared spectra are now available for JWST data analyses (Terwisscha van Scheltinga et al. 2018, 2021; Rachid et al. 2020, 2021, 2022; Hudson & Gerakines 2019; Hudson & Ferrante 2020; Hudson et al. 2021; Hudson & Yarnall 2022; Gerakines et al. 2022; Rocha et al. 2022). The ultimate goal is to bridge the gas and grain chemistries and directly relate gas-phase spectra as presented here to solid-phase infrared features, from which we can gain a better understanding about the formation history of COMs.

2. Observations

2.1. Overview

This paper presents early results from a first look at data from the CoCCoA survey (PI: B. McGuire). A complete overview of the survey will be provided in a separate publication once all observations are complete. This will be followed by the public release of fully reduced spectral-line image cubes. When complete, CoCCoA will comprise a dataset targeting 23 high-mass star-forming regions at a spatial resolution of ~0.3″ using multiple configurations of the ALMA 12-m array as well as the ALMA 7-m array to capture both extended and compact emission. The CoCCoA survey will ultimately include data from ALMA projects 2019.1.00246.S, 2019.2.00112.S, and 2022.1.00499.S.

The sources were chosen to be within ~1–4 kpc, corresponding to a linear-scaled spatial resolution of ~300 to 1200 au at the nominal 0.3″ angular resolution. Other than this distance requirement, the only other criterion used for selection was that the sources have a prior literature report of "hot core chemistry," either described as such or evidenced by the presence of a rich array of emission lines of methanol and other COMs. The goal is to provide a diverse dataset in order to better sample the phase space of chemical complexity and avoid biases toward the chemistry seen in the commonly observed extraordinary sources such as Sgr B2 (see, e.g., El-Abd et al. 2019).

The observations cover two spectral tunings per source in Band 6. The lower tuning covers 238.0–241.7 GHz, while the upper tuning covers 258.0–261.7 GHz. All observations are taken with 0.488 MHz spectral resolution (twice the channel width due to online Hanning smoothing), corresponding to ~0.6 km s^{-1}. These frequency ranges were chosen to maximize both the number of transitions and the range of upper-state rotational energy levels of key target molecules, including those highlighted here. These first-look results use data from the upper tuning (258.0–261.7 GHz), for which observations have been completed for 14 total sources, listed in Table 1.

2.2. Data reduction

The 12m array CoCCoA data presented here from project 2019.1.00246.S were observed between March 24, 2021, and April 2, 2021, using configuration C-5. The data were calibrated using the Cycle 8 version of the ALMA Pipeline (CASA version 6.2), including corrections for renormalization issues larger than 2%. Due to the copious line emission emanating from the massive protostars within each targeted cluster, the default parameters of the `findContinuum.py` procedure used by the pipeline to identify line-free channels did not yield optimal results (i.e., significant line contamination was present). Therefore, `findContinuum.py` (available in the `extern` directory of the pipeline distribution) was run manually with a few key parameters (primarily `sigmaFindContinuum`[1]) adjusted in order to minimize the line contamination.

After optimization of the channels used for continuum subtraction, the line-free channels were used to image the continuum and perform an iterative self-calibration (Brogan et al. 2018). The self-calibration solutions were also applied to the continuum-subtracted line datasets. The imaging of both the continuum and data cubes employed the `multiscale` functionality of CASA's `tclean` with scales of 0, 5, and 15 (the `cellsize` was chosen to oversample the beam on the smallest axis by a factor of ~5). The `robust` parameter employed is 0.5, which yielded an angular resolution near 0.3″; both the continuum and line images were subsequently convolved to exactly 0.3″. The maximum recoverable scale of these data is ~2.5″.

Considering that the data in the lower tuning are still under reduction, only the upper tuning was used for further analysis. The quality of the ALMA pipeline data of the lower tuning is good enough to see how many COM lines are included in each tuning. Among the 14 sources, we took G19.88-0.53 as an example for line identification, since its spectrum shows less line blending despite the large line intensities. This ensured a sufficiently large number of detected lines without suffering too much from blending issues. The upper tuning covers about 70% of the COM lines found in both tunings (not including CH_3OH), while the lower one is more abundant in strong lines of CH_3OH and CH_3CN, which are not directly relevant to our project. Therefore, we consider our results to be robust using only the data in the upper tuning.

3. Methods

3.1. Spectral analyses

Figure 1 shows the continuum maps and the integrated intensity (moment 0) maps of the CH_3OH $19_{3,17}$–$19_{2,18}$ transition with upper energy E_{up} = 490 K and Einstein A coefficient $A_{ij} = 9.27 \times 10^{-5}$ s^{-1}. This particular methanol line was chosen because it is unblended and has the lowest E_{up} and the highest A_{ij} in the upper tuning, which is expected to show the most extended methanol emission. Figure 2 presents an overview of the spectra in the upper tuning, with several representative line features of MF and DME indicated by shaded areas. The spectra were extracted from the peak pixel of the methanol intensity maps. The moment 0 maps of other selected O-COMs of one example source G19.88-0.53 are shown in Fig. A.1, which confirmed that their emission peaks at similar regions to the methanol emission. In most sources, the methanol emission peaks at the same location as the continuum. However, in some bright sources, such as G34.30+0.20 (Fig. 1), the methanol emission shows a ring shape

[1] The `sigmaFindContinuum` parameter sets how far above the corrected median of the baseline channels to place the initial threshold (the baseline channels, `nBaselineChannels`, were drawn from the lowest 10% of channels after excluding outliers). The `narrow` parameter was also set to two, instead of the default of four, in order to preserve as many narrow windows as possible.

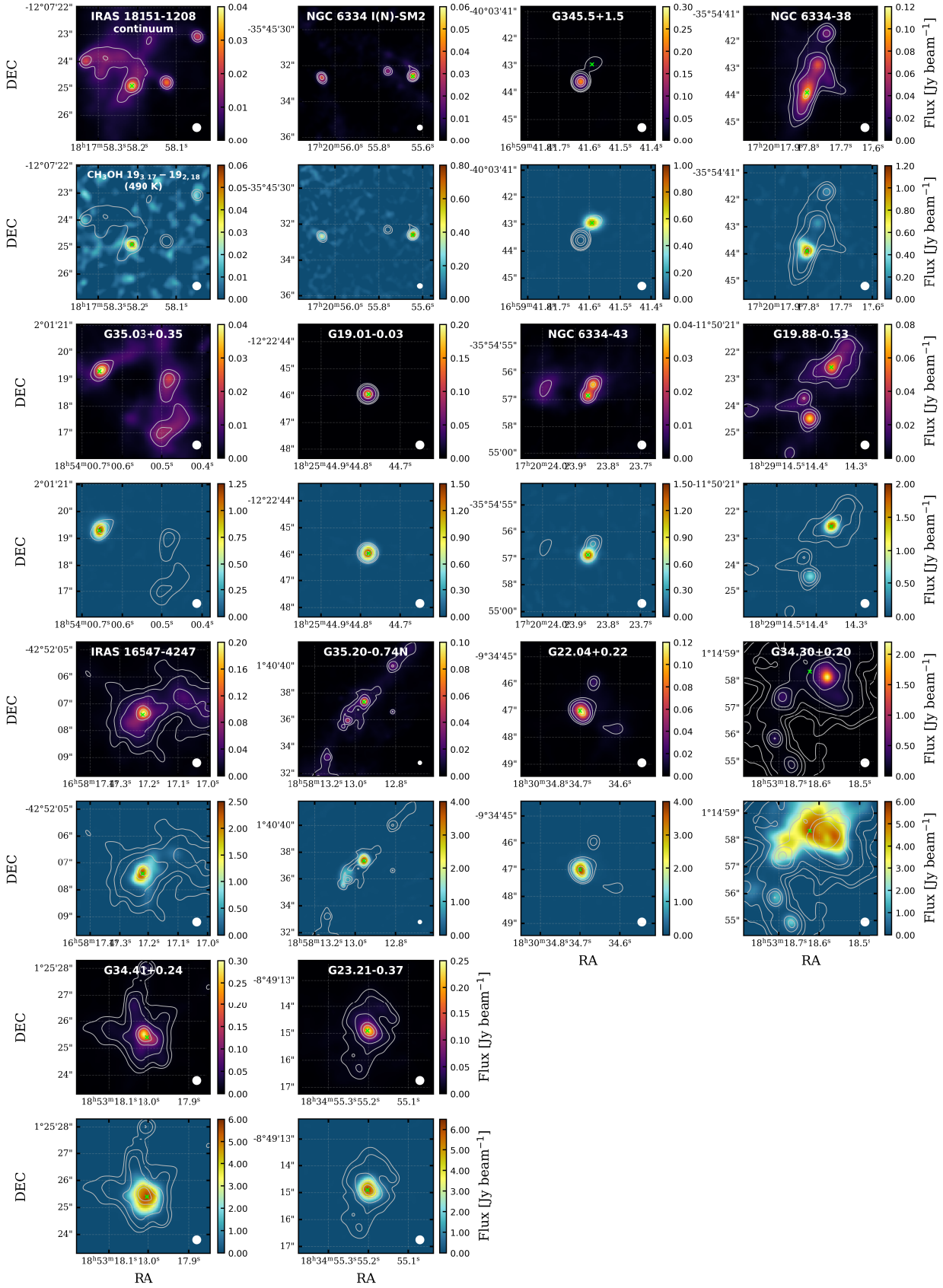

Fig. 1. Continuum maps (odd rows, black-yellow) and moment 0 maps of the methanol line at 258.78 GHz ($19_{3,17}$–$19_{2,18}$) with E_{up}= 490 K (even rows, blue-red) for the 14 high-mass CoCCoA sources. The white contours indicate the continuum emission at the 3, 5, 10, 30, 50, and 100σ level (σ = 0.03 mJy beam^{-1}). The peak pixels from where the spectra were extracted are marked by crosses in light green. The sources are sorted by peak flux of methanol emission. The beam size (0.33″) is denoted by white ellipses in the lower right of each panel. The field of view for NGC 6334 I(N)-SM2 and G35.20-0.74 N is set to be twice as large as that of others in order to include more emission peaks.

Table 1. Names, phase center coordinates, coordinates where spectra were extracted, and properties of sources analyzed.

Source name[‡]	Phase center[†] RA	Phase center[†] Dec	Extraction location[†] RA	Extraction location[†] Dec	L (10^4 $L_\odot$)	D (kpc)	D_{GC} (kpc)	$^{16}O/^{18}O$	Refs.
G19.01-0.03	18:25:44.80	–12:22:45.8	18:25:44.78	–12:22:45.95	1	4.0(3)	4.4	298 ± 52	*L*: 1, *D*: 2
G19.88-0.53	18:29:14.57	–11:50:23.0	18:29:14.36	–11:50:22.50	0.47	3.31	5.1	335 ± 60	*L*: 3, *D*: 4
G22.04+0.22	18:30:34.70	–09:34:47.0	18:30:34.70	–09:34:47.00	0.497(26)	3.4(5)	5.0	333 ± 60	*L*: 5, *D*: 5
G23.21-0.37	18:34:55.26	–08:49:15.3	18:34:55.20	–08:49:14.70	1.3	4.6	4.2	286 ± 50	*L*: 6, *D*: 6
G34.30+0.20	18:53:18.54	+01:14:57.9	18:53:18.62	+01:14:58.35	4.6	1.6	6.8	436 ± 80	*L*: 7, *D*: 7
G34.41+0.24	18:53:17.90	+01:25:25.0	18:53:18.02	+01:25:25.15	0.48	1.6	6.8	436 ± 80	*L*: 8, *D*: 8
G35.03+0.35	18:54:00.50	+02:01:18.0	18:54:00.66	+02:01:19.30	0.63	2.32	6.3	407 ± 74	*L*: 9, *D*: 10
G35.20-0.74N	18:58:13.00	+01:40:36.5	18:58:12.96	+01:40:37.35	3	2.2(2)	6.4	411 ± 75	*L*: 11, *D*: 12
G345.5+1.5	16:59:41.63	–40:03:43.6	16:59:41.59	–40:03:42.90	4.8	1.5	6.6	426 ± 78	*L*: 13, *D*: 13
IRAS 18151-1208	18:17:58.00	–12:07:27.0	18:17:58.22	–12:07:24.90	2.2	2.9	5.4	353 ± 63	*L*: 14, *D*: 14
IRAS 16547-4247	16:58:17.20	–42:52:07.0	16:58:17.22	–42:52:07.35	6.3	2.9	5.3	353 ± 63	*L*: 13, *D*: 13
NGC 6334-38	17:20:18.00	–35:54:55.0	17:20:17.80	–35:54:43.85	<20	1.7	6.4	412 ± 75	*L*: 15, *D*: 15
NGC 6334-43	17:20:23.00	–35:54:55.0	17:20:23.86	–35:54:56.90	<20	1.7	6.4	412 ± 75	*L*: 15, *D*: 15
NGC 6334 I(N)-SM2	17:20:55.00	–35:45:40.0	17:20:55.64	–35:45:32.60	0.07	1.3(1)	6.8	434 ± 79	*L*: 16, *D*: 17

Notes. [†]Coordinates given in J2000; Right Ascension (RA) in units of °:′:″; Declination (Dec) in units of hh:mm:ss. [‡]Other names exist for many of these, including different designations for the larger star-forming complex and for individual sub-sources within the complex.

References . [1] Cyganowski et al. (2011), [2] Williams et al. (2022), [3] Issac et al. (2020), [4] Ge et al. (2014), [5] Towner et al. (2021), [6] Tang et al. (2018), [7] Csengeri et al. (2022), [8] König et al. (2017), [9] Beltrán et al. (2014), [10] Wu et al. (2014), [11] Sánchez-Monge et al. (2013), [12] Zhang et al. (2009), [13] Faúndez et al. (2004), [14] Maud et al. (2015), [15] Widicus Weaver et al. (2017), [16] Sandell (2000), [17] Chibueze et al. (2014).

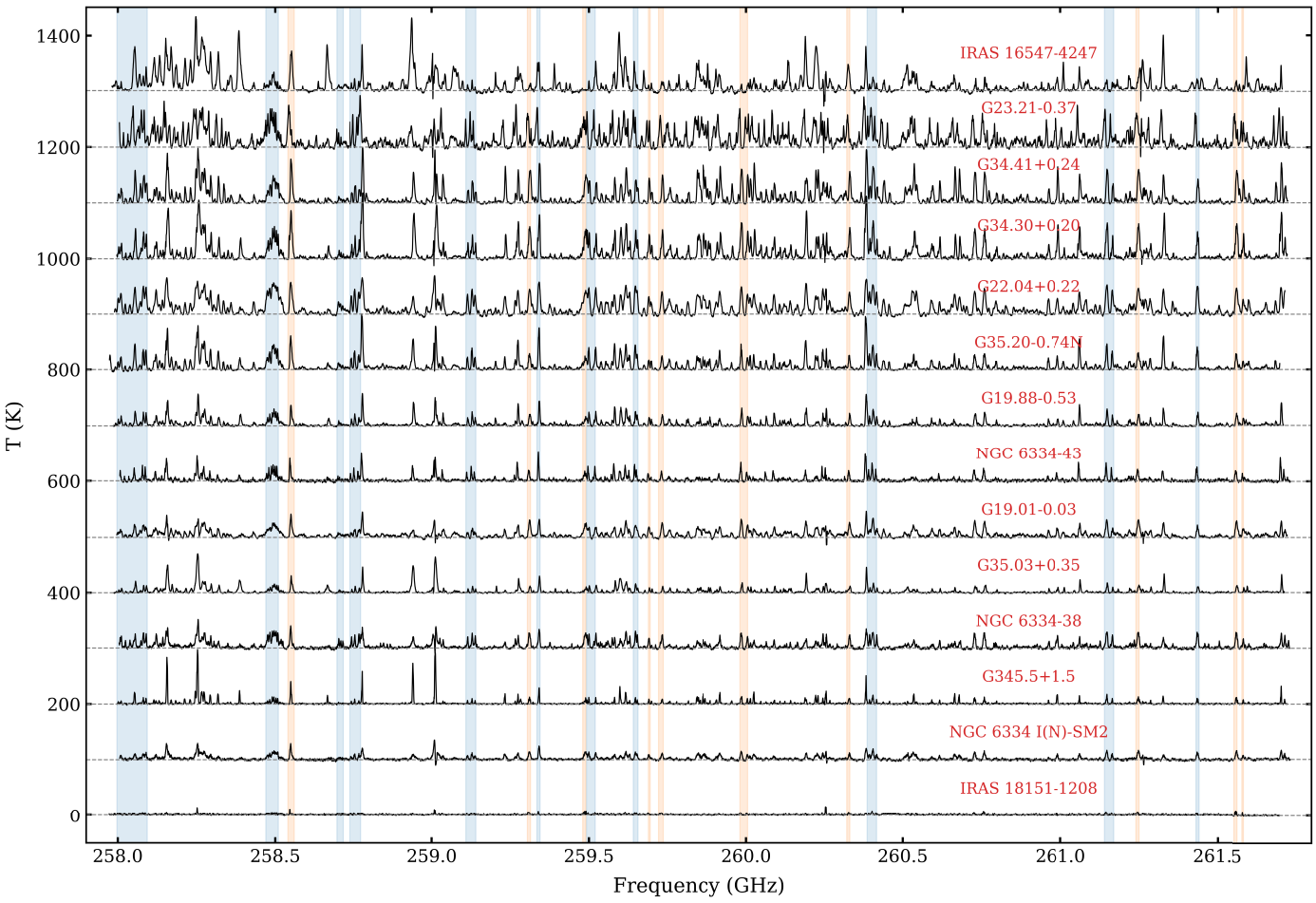

Fig. 2. An overview of the spectra in the upper tuning (258.0–261.7 GHz) of the 14 high-mass sources observed in the CoCCoA survey. The line intensity has been converted from flux in Jansky per beam to brightness temperature in Kelvin using the Rayleigh-Jean approximation. The spectra are sorted by the average line intensities from bottom to top, and each one is offset by 100 K. The shaded regions in blue and orange indicate the emission lines of MF and DME, respectively.

around the continuum peak, which is likely due to the high optical depth of dust (De Simone et al. 2020; van Gelder et al. 2022). In this case, we picked the brightest pixel on the ring to extract the spectra. For the two bright sources G34.41+0.24 and G23.21-0.37, the methanol emission peaks at the same location as the continuum, but the spectrum extracted from the central pixel has too much line blending, so we deliberately chose a pixel offset from the actual peak (∼9 pixels offset for G34.41 and ∼3 pixels offset for G23.21).

After extracting all the spectra, we performed line identification and spectral fitting using the spectral analysis software CASSIS[2] (Vastel et al. 2015). The spectroscopic data in CASSIS are taken from two databases: the Jet Propulsion Laboratory database (JPL; Pickett et al. 1998) and the Cologne Database for Molecular Spectroscopy (CDMS; Müller et al. 2001, 2005; Endres et al. 2016). Detailed references for each species can be found in Appendix A of van Gelder et al. (2020). Some species only have data available in one database, while others are included in both databases. In the latter case, we used either the database with smaller uncertainties in the central frequency or that has been used more frequently in previous work. We first went through the detection inventory of the PILS survey (Jørgensen et al. 2016) and checked whether all the transitions in the databases have corresponding line features in the observed spectra for each species. The detection results are presented in Sect. 4.2.

In the next step, we chose the six O-COMs and the two methanol isotopologues ($^{13}CH_3OH$ and $CH_3^{18}OH$) mentioned in Sect. 1 for detailed spectral fitting using CASSIS. The two conformers of EG (*a*-EG and *g*-EG) were fit separately due to their different sets of transitions. The column density (N), excitation temperature (T_{ex}), and full width half maximum (FWHM) of each molecule were fit for each source. We assumed one T_{ex} for each species; that is, the populations of all levels can be characterized by a single T_{ex}, which is often called "local thermodynamic equilibrium (LTE)" in radio astronomy. However, the LTE here does not necessarily refer to its strict definition that T_{ex} approaches the kinetic temperature T_{kin} under high-density conditions. In fact, COMs are likely to be subthermally excited ($T_{ex} < T_{kin}$) in hot cores, while the observed lines can still be well characterized by one T_{ex}. Examples provided in Fig. 6 of Johnstone et al. (2003) and Fig. 8 of Jørgensen et al. (2016) show that for the case of methanol, densities of 10^9–10^{10} cm^{-3} are needed for thermalization. Correspondingly, physical models of the envelopes of high-mass protostars (e.g., van der Tak et al. 2013) indicate densities of 10^7–10^9 cm^{-3} at temperatures of 100–300 K on scales of a few hundred au. At such densities, the level populations of COMs may not yet be fully in LTE, while the fitting results in Sect. 4 show that the single-T_{ex} assumption is reasonable and works well.

We adopted two methods for fitting the spectra: χ^2 minimization and visual inspection, when the former was not applicable. For each source, the radial velocity v_{lsr} and FWHM were determined for each species based on strong unblended lines. The uncertainties of v_{lsr} and FWHM are smaller than 0.5 km s^{-1}. The difference of v_{lsr} among the O-COMs is within 1 km s^{-1} in most cases. For sources where the lines are narrow and unblended, grid-fitting was used to determine the best-fit values as well as the uncertainties by calculating χ^2 in the parameter space and making the contour plot on the N–T_{ex} plane (also see Sect. 3.1 in van Gelder et al. 2020). For each species, χ^2 was calculated from the difference between the LTE model and the observed spectrum around unblended lines. We started with a sparse grid with broad ranges of N, T_{ex}, and FWHM and large intervals between the grid points. We then gradually narrowed down to smaller ranges and smaller intervals. Finally, we ended up with a fine grid around the best-fit grid point, from which we could make the contour plot and estimate the 2σ uncertainties. This grid-fitting method works well with weaker sources where most of the lines are unblended. However, for bright sources where the lines are very broad and blended, grid-fitting does not converge to a solution and the results need to be visually inspected.

When it came to fitting by visual inspection, we started with an initial guess of the parameters and adjusted them to a better fit until no improvement could be made. This is more efficient and reliable for complex spectra with blended lines since we can monitor the change intuitively and interactively. This method was also adopted by van Gelder et al. (2020) and Nazari et al. (2021, 2022a). Uncertainties were estimated by comparisons shown in Fig. A.2, in which the three panels correspond to the lower limit, the best fit, and the upper limit. Panel (a) shows that with an underestimated T_{ex}, low-E_{up} transitions tend to overestimate the observation, while in panel (c), high-E_{up} lines are overestimating the observation with an overestimated T_{ex}.

In some cases, grid-fitting did not work well for T_{ex}, even when there are enough unblended lines available for a certain species. This is because a robust estimation on T_{ex} requires the unblended lines to cover a wide range of E_{up} so that the models can be sensitive to temperature changes. For species such as $CH_3^{18}OH$, GA, and *g*-EG, there are few unblended lines covering a wide range of E_{up}. These lines are either too weak to be detected in faint sources or severely blended by strong lines in bright sources. Under these circumstances, the results of grid-fitting will not be able to constrain the T_{ex}, as it is often accompanied by huge uncertainties. As a solution, we fixed T_{ex} to be equal to that of MF, which has the most identified transitions and therefore the best constraint on T_{ex}, and only N was fit and estimated for uncertainties. Nevertheless, the T_{ex} of *g*-EG is always set to be the same as that of *a*-EG. We consider the fitting results of N to still be representative since the difference would be within a factor of two if we changed the fixed value of T_{ex} by 20–50 K in the range of 100–250 K, which is a typical temperature range for hot cores (e.g., Fig. 2 in Ligterink et al. 2015). Similarly, if the FWHM could not be constrained to better than 0.5 km s^{-1} uncertainty due to the blending of lines, it was also fixed to a value (e.g., if the possible range is 3.5–4.0 km s^{-1}, we used 3.8 km s^{-1}).

Additionally, there are two special cases that we encountered during the fitting. One is that the spectra of several sources (i.e., G19.01-0.03, G34.30+0.20, G34.41+0.24, and G35.20-0.74N) show double-peaked line profiles in some O-COMs, which cannot be fit with only one component. These double-peaked features appear in nearly all the transitions and are thus unlikely to be due to self-absorption. An example of two-component fitting is given by Fig. A.3, which shows that the spectra can be well fit by two components with different v_{lsr} and N, `whereas` T_{ex} remains the same (see Tables B.1–B.5 for relevant sources and species). It is likely that these sources are not spatially resolved (e.g., maps of G19.01-0.03 show a perfect beam shape in Fig. 1), and there is more than one physical component contained in the beam. The second case is that in the two sources G23.21-0.37 and NGC 6334-38, we found the MF lines to be highly optically thick. All strong lines with $A_{ij} \gtrsim 10^{-4}$ s^{-1} are saturated and therefore do not show correct intensity ratios against weaker lines. In this case, the fitting was only based on weak lines with $A_{ij} < 10^{-4}$ s^{-1}.

[2] http://cassis.irap.omp.eu/

3.2. Isotope ratio calibration for methanol

As mentioned in Sect. 3.1, the column density of CH_3OH needs to be inferred from its minor isotopologues since the main isotopologue itself is likely to be optically thick. The isotope ratios of $^{16}O/^{18}O$ and $^{12}C/^{13}C$ can be calculated from the distance to the Galactic center (D_{GC}) using the equations in Wilson & Rood (1994) and Milam et al. (2005):

$$(^{16}O/^{18}O) = (58.8 \pm 11.8)D_{GC} + (37.1 \pm 82.6) \quad (1)$$

$$(^{12}C/^{13}C) = (6.21 \pm 1.00)D_{GC} + (18.71 \pm 7.37), \quad (2)$$

where D_{GC} can be derived from the coordinates of the sources and their distances to Earth. The two values before and after D_{GC} (with uncertainties) are the slope and intercept of these linear relationships, respectively. In the vicinity of the solar system, D_{GC} is 8.05 kpc, which gives $^{16}O/^{18}O \sim 510$ and $^{12}C/^{13}C \sim 69$. In the literature, 560 and 70 are commonly used for nearby low-mass sources. For the high-mass sources that are farther away from the solar system, isotope ratios can be calculated from D_{GC} before applying them to infer the column density of $^{12}CH_3^{16}OH$ (Table 1). If both $^{13}CH_3OH$ and $CH_3^{18}OH$ are optically thin, we can expect their column density ratio to be 7–8. However, our fitting results show a ratio of 2–5, which indicates that $^{13}CH_3OH$ is also (marginally) optically thick. Therefore, only $CH_3^{18}OH$ is used to calculate the column density of methanol.

If the errors of both the slope and the intercept are considered in error propagation, the uncertainties of $^{16}O/^{18}O$ would be around 30% of the ratios themselves (e.g., if $^{16}O/^{18}O = 300$, the error will be ~90). However, a large portion of the total uncertainty comes from the intercept error (82.6), which is even two times larger than the intercept itself (37.1). Considering that only the slope in Eq. (1) contains the information of the trend between the $^{16}O/^{18}O$ ratio and D_{GC} and that the intercept error only represents the scatter of the sources from which the equation was originally fit, we did not include the intercept error in the error propagation. This yielded a decrease in the uncertainties of $^{16}O/^{18}O$ from ~30% to ~18%. Results that include the intercept error are shown in Fig. A.4.

4. Results

4.1. Morphology

The continuum maps of the 14 CoCCoA sources show different morphologies (see odd rows in Fig. 1). Six out of the 14 sources show a single peak in both continuum and methanol emission. Others have multiple peaks in continuum but only one or two peaks in methanol emission, usually corresponding to the brightest continuum peak(s). The source G345.5+1.5 is an exception in that its methanol peak is offset from the continuum peak, and the corresponding region in continuum does not show a peak feature. The source G35.20-0.74N is an interesting source, as the four continuum peaks are located along a line and the methanol emission tends to follow the same alignment. Except for several sources that are not well resolved, most sources show extended weak continuum emission aside the flux peaks, implying the existence of dusty envelopes or parent cores. More detailed studies on the morphology of CoCCoA sources will be presented in a future paper.

4.2. Spectra and detection

As expected from the selection of sources and frequency range, the extracted spectra are rich in COM lines for all the 14 sources in the upper tuning. An overview of the full spectra of each source is presented in Fig. 2. We observed that the spectral appearance of our sources is diverse in intensities and line widths. Bright sources such as G34.41+0.24 and G23.21-0.37 have very strong and broad lines ($\gtrsim$5 km s^{-1}) that are severely blended and can only be fit by visual inspection. There are also faint sources, such as IRAS 18151-1208 and NGC 6334 I(N)-SM2, where the lines are much weaker and narrower (<2 km s^{-1}). Their spectra are clean enough for χ^2 fitting, but some less abundant species and some weak lines (with lower A_{ij}) may remain undetected. The spectra of the other sources have intermediate intensities and line widths (3–4 km s^{-1}), which are easiest to fit.

The 14 sources provide a rich inventory of detections. More than ten O-bearing COMs and about five N-bearing species are detected in the upper tuning. These detections include the originally targeted species as well as other O- and N-bearing species, covering alcohols, aldehydes, esters, ethers, ketones, acids, and the simplest sugar (GA). We did not detect methoxymethanol (CH_3OCH_2OH) since our frequency range only covers its weak lines with $A_{ij} < 10^{-5}$ s^{-1}, and no corresponding line features were spotted in the spectra. Besides the COMs mentioned above, two simple O-bearing molecules, ketene (H_2CCO) and formic acid (t-HCOOH), have one and three transitions covered in the upper tuning, respectively. The N-bearing species include HNCO, CH_3CN, C_2H_5CN, and NH_2CHO. Some abundant species such as HNCO and CH_3CN also have their ^{13}C isotopologues detected. A hydrocarbon molecule, propyne (CH_3CCH), is also detected but with all its transitions covered in the lower tuning. Simpler molecules such as SiO, SO, and SO_2 only have very few strong lines covered in the upper tuning and do not affect our analysis on O-COMs. Species detected in the CoCCoA sources but not the focus of this paper will be studied in future works.

Figure 3 shows the best-fit model of G19.88-0.53 in a line-rich frequency range (259.4–260.6 GHz). A version for the full upper tuning is given by Fig. A.5, and Figs. A.6–A.8 show zoom-in panels for selected unblended lines of each species. The model contains the minor isotopologues of methanol and the six O-COMs that we focus on in this paper. More than 70% of the line features can be fit quite well with uncertainties of less than 30%, assuming a single excitation temperature. Apart from several strong features that are attributed to the main isotopologue of methanol and some simple molecules (e.g., SO and SO_2), weaker features that are not well fit by the model likely originate from other COMs that are not included in the model, such as acetone (CH_3COCH_3), N-bearing COMs, and some minor isotopologues of the detected species. The identified transitions of the selected O-COMs are listed in Table B.6, where transitions that are above 3σ and not fully blended with other strong lines are considered as "identified." We observed that most of the identified transitions have an upper energy level of 100–300 K.

4.3. Column density and excitation temperature

The column densities and excitation temperatures of all sources are presented in Tables B.1–B.4. Vibrational corrections have been applied to the column densities of GA and EG (more information can be found in Sect. 5 of Jørgensen et al. 2016), and the column densities without vibrational corrections are provided in Table B.5. With the uniform beam size of 0.33″, most sources have a methanol column density of 10^{18}–10^{19} cm^{-2}, except the weakest source IRAS 18151-1208, which has $N = 7 \times 10^{17}$ cm^{-2}. Among the six O-COMs that we focus on (excluding

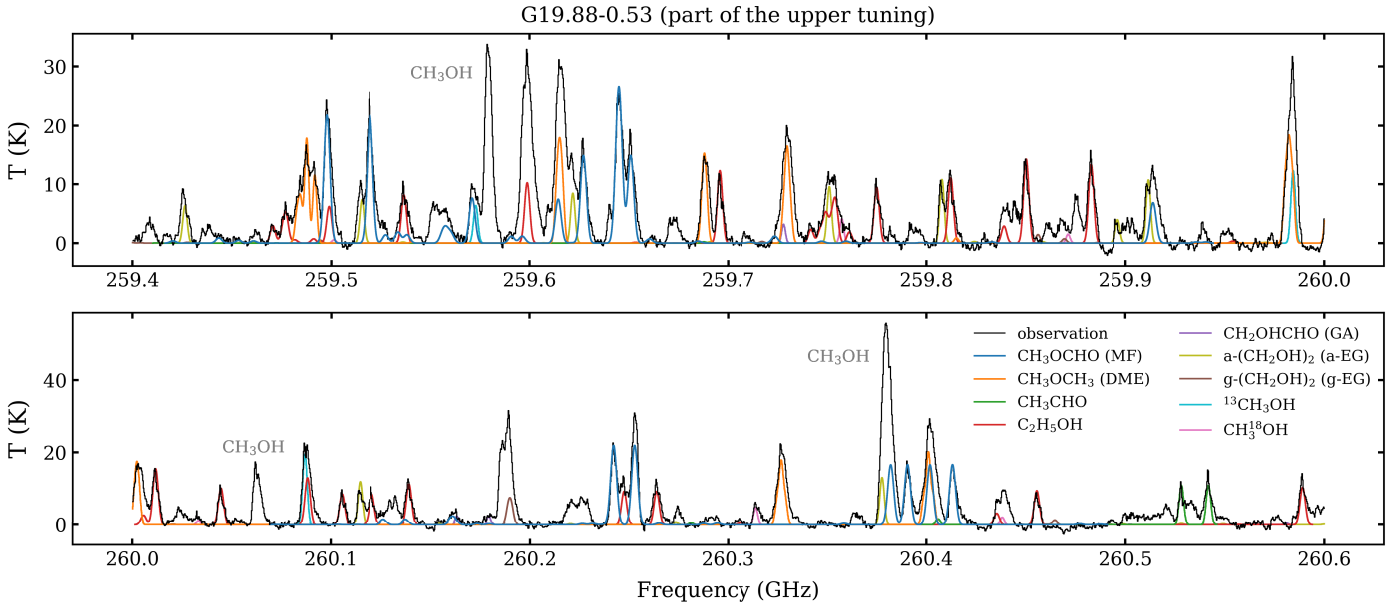

Fig. 3. Best fit of the observed spectrum of G19.88-0.53 in a line-rich frequency range (259.4–260.6 GHz). The black and colorful spectra correspond to the observed spectrum and the modeled spectra of each species, respectively. Only the O-bearing COMs targeted in this paper (excluding CH_3OH) are shown here. Two strong lines of methanol are labeled in gray text in the panels. The same figure but for the full upper tuning is given in Fig. A.5.

methanol isotopologues), DME and MF are the most abundant, with column densities about one order of magnitude higher (10^{16}–10^{17} cm^{-2}) than those of the other four species. These two species always have a considerable number of strong lines available for fitting in the spectra of all sources (as shown by the shaded areas in Fig. 2). C_2H_5OH has somewhat fewer distinct transitions (unblended and large A_{ij}), and it is not always abundant enough to produce strong lines. In some sources, the column density of C_2H_5OH is of the same order of magnitude as DME and MF, while in some other sources the difference can reach up to two orders of magnitude. This big variation is also present for a-EG, which has many strong transitions covered in our data. In some sources, the number of detected lines of a-EG are as high as those of DME, while in others there are only a few obvious line features. The fitting of GA and g-EG is more difficult since they only have two to three distinct transitions, which are often subject to blending issues. In summary, the average column densities of the six O-COMs rank as DME ~ MF > C_2H_5OH > (a+g)EG > CH_3CHO > GA. Since the absolute values of N are related to the physical environments of the parent sources, it is more useful to look at the relative abundances of O-COMs, that is, their column density ratios with respect to methanol (see Sect. 5 for details).

As for the excitation temperature, C_2H_5OH, MF, and a-EG tend to have a warm T_{ex} of $\gtrsim$150 K, while CH_3CHO and DME have a relatively lower T_{ex} of 100–130 K. This may be because different species have a different emitting area of the hot core. For example, some species are emitting from a slightly colder and more extended region, which is not well resolved in our sample according to Fig. A.1). Hot cores are known to have temperature gradients (e.g., van der Tak et al. 1999, 2000; Beltrán et al. 2018; Gieser et al. 2019), but they are only probed on scales larger than the observing beams. Since our analyses are based on the spectra at the peak pixels, the temperature structure on larger scales is not expected to affect our results. The lower T_{ex} of CH_3CHO and DME is also consistent with earlier single-dish findings of other high-mass sources (Bisschop et al. 2007; Isokoski et al. 2013) and the results of low-mass sources in van Gelder et al. (2020). As mentioned in Sect. 3.1, $CH_3^{18}OH$, GA, and g-EG usually have fixed T_{ex} due to a lack of unblended lines covering a wide range of E_{up}.

5. Discussion

5.1. Column density ratios

To further investigate the COM chemistry in our sample, we calculated the column density ratios of O-COMs with respect to methanol, and we summarize these column density ratios in Fig. 4. The column densities of the two conformers of EG (a-EG and g-EG) are summed up in the last subplot, although they were fit separately. The uncertainty of the column density ratios was propagated from the uncertainties of the O-COM column densities and the $^{16}O/^{18}O$ ratio (calculated in Sect. 3.2) of each source. In Fig. 4 we also compare our observational results of high-mass protostellar sources with the results of low-mass sources in literature (Jørgensen et al. 2018; Manigand et al. 2020; van Gelder et al. 2020) and the simulation results of COM chemistry in Garrod et al. (2022). For consistency, this figure does not include results of other COM observations (e.g., Csengeri et al. 2019; Yang et al. 2021), as they did not use minor isotopologues to derive the column density of methanol as we did.

Figure 4 shows that there is no obvious difference in the O-COM ratios between low-mass and high-mass sources. However, molecules in the two groups should have experienced different physical conditions, such as temperature and fluence of energetic particles (UV photons, X-rays, cosmic rays) before the hot cores and hot corinos formed. This implies that these species are likely formed under similar conditions, which points to a common and early pre-stellar stage before the star formation processes began to differentiate.

The six selected O-COMs have different column density ratios with respect to methanol, varying by over two orders of magnitude between 0.01% and 10%. Among the six species,

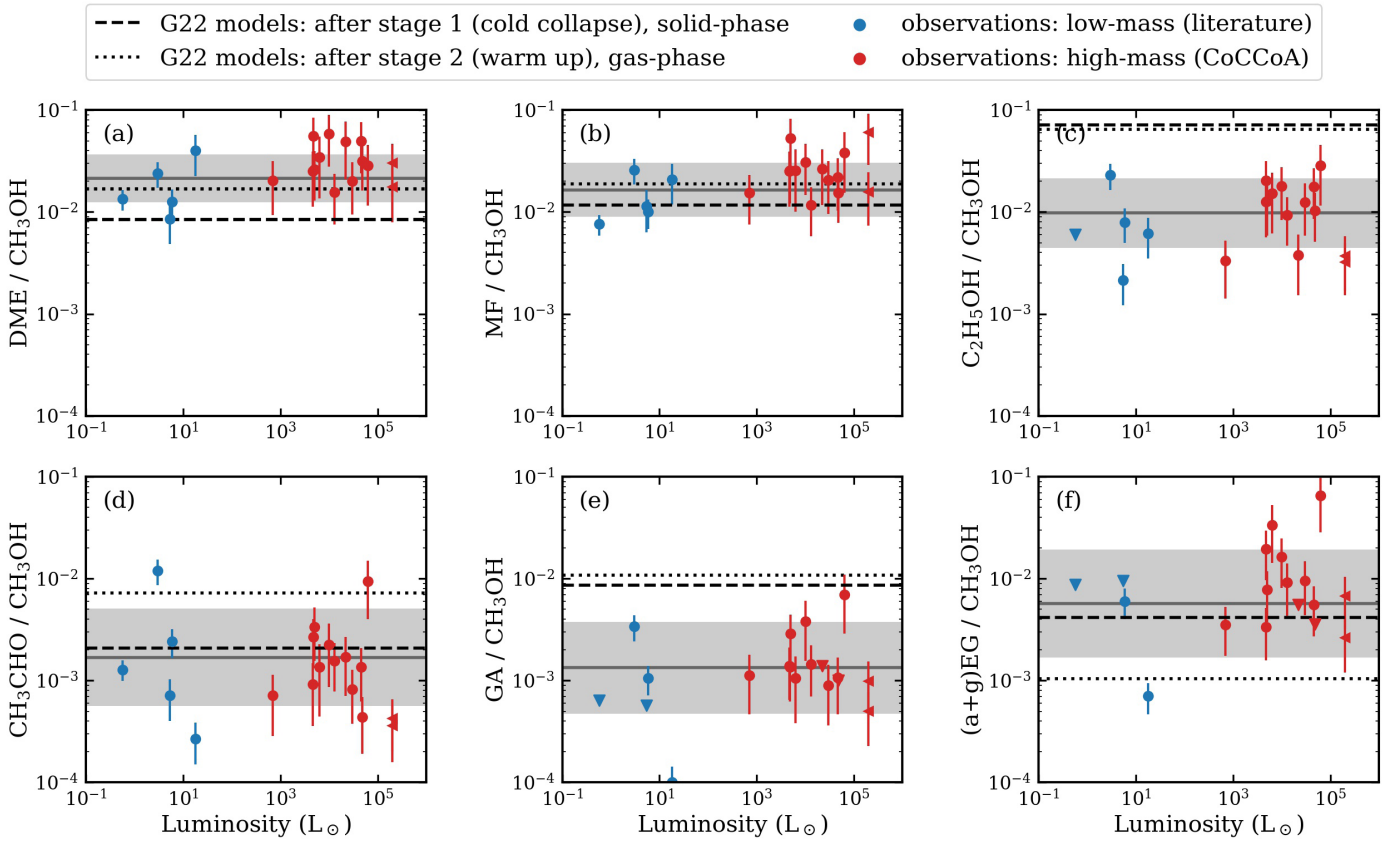

Fig. 4. Column density ratios of six O-COMs with respect to methanol versus bolometric luminosity. Panels from left to right and top to bottom: dimethyl ether (DME; CH_3OCH_3), methyl formate (MF; CH_3OCHO), ethanol (C_2H_5OH), acetaldehyde (CH_3CHO), glycolaldehyde (GA; CH_2OHCHO), and ethylene glycol (EG; $(CH_2OH)_2$). The red points show the CoCCoA data of 14 high-mass sources derived in this work, and the blue points show the literature data of five low-mass sources: IRAS 16293-2242 A & B (Manigand et al. 2020; Jørgensen et al. 2018), S68N, B1c, and B1-bS (van Gelder et al. 2020). Upper limits are denoted by downward triangles. The data points of NGC 6334-38 and NGC 6334-43 are denoted by leftward triangles due to their upper limits on luminosity. The solid line in gray corresponds to the mean column density ratio of each species, and the gray shaded area shows the standard deviation weighted by the uncertainty on log scales. The mean and standard deviation were calculated from both the high-mass sources and the low-mass ones. The dashed and dotted lines in black correspond to the modeled COM ratios at the end of the cold collapse stage (stage 1) and the warm-up stage (stage 2) in G22, respectively.

DME and MF have the highest and similar ratios with respect to methanol (2–3%); C_2H_5OH and EG have intermediate ratios but with a much larger scatter; and CH_3CHO and GA have the lowest ratios, at around 0.1%.

Figure 5 shows the spread factor, that is, $\log_{10}$ of the standard deviation of O-COM ratios in log scales, of our combined sample of low-mass and high-mass protostars. It is clear that DME and MF have smaller scatter than the other four species. The scatter may result from an observational effect that different species have different gas-phase emitting areas depending on their sublimation temperatures from dust grains (Nazari et al. 2021, 2022a). The column densities that we derived from spectral fitting represent the abundances averaged over the observational beam. If the actual emitting area of a species is smaller than the area that we can resolve, then we suffer from a beam dilution issue. This is likely the case in the CoCCoA observations since the moment 0 maps of selected O-COMs given in Fig. A.1 show that the emission of these molecules are barely or not spatially resolved. The actual resolved area associated with a specific beam size depends not only on the angular resolution (which is constant across the CoCCoA sample) but also on the distance to a source (which varies by a factor of three to four across the sample). Moreover, the size of the hot core, as defined by the radius where T = 100 K, depends on the square root of the luminosity of the source (Bisschop et al. 2007):

$$R_{T=100\ \mathrm{K}} \approx 15.4 \sqrt{\frac{L}{L_\odot}}\ \mathrm{au}. \quad (3)$$

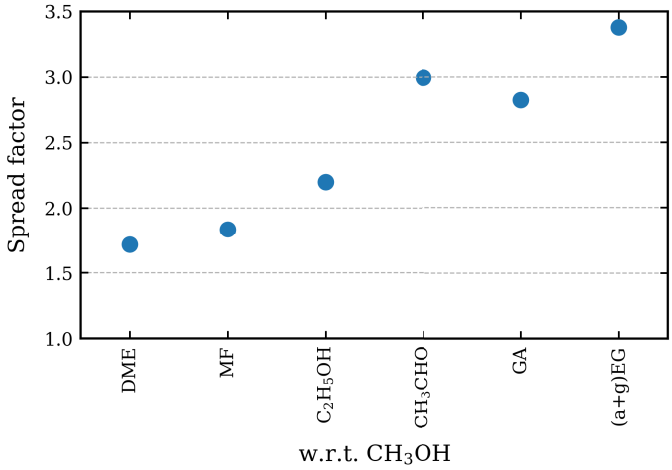

Fig. 5. Spread factor ($\log_{10}$ of the 1σ scatter) for the ratios plotted in Fig. 4 of different O-COMs with respect to methanol.

Therefore, there is a beam dilution factor between the observationally inferred column density and the actual one. This factor can differ from source to source and from species to species, and hence, it can lead to the scatter in COM ratios. These effects are discussed and quantified in more detail in Nazari et al. (2022b, 2023).

More generally, we note that surveys of large samples of low- and high-mass protostars have found that some fraction of sources do not show any methanol or COM emission (e.g., Yang et al. 2021; van Gelder et al. 2022, Paper I). The reasons for this absence of COM emission are varied but include the possible presence of a disk that lowers the overall temperature structure (Nazari et al. 2022b, Paper II) as well as different evolutionary stages, such as the presence of an H II region (Nazari et al. 2023, modeling paper).

5.2. Observations versus simulations

The simulations used to compare with our observational results are mainly based on the state-of-the-art models in Garrod et al. (2022, hereafter G22). The G22 models simulate the chemistry coupled in three phases: gas phase, ice surface, and bulk ice mantle. The last two phases are collectively known as the solid phase. The evolution of hot cores is treated as two stages, a cold collapse stage followed by a static (fixed density) warm-up stage once the central protostar has formed. There are three warm-up timescales used in the models: 5×10^4 yr (fast), 2×10^5 yr (medium), and 1×10^6 yr (slow). A major update in the G22 models involves including non-diffusive chemistry on surfaces and in bulk ices, which is proposed to be important in interstellar ices based on laboratory work (Fedoseev et al. 2015; Linnartz et al. 2015). The G22 test the effect of different non-diffusive mechanisms along with other parameters in about 20 models (see Table 1 in G22). The "final" model includes all the discussed non-diffusive mechanisms, and we used it as the fiducial model for further discussion. In Fig. 4, the horizontal dashed lines correspond to the COM ratios (w.r.t. methanol) in the solid phase at the end of the collapse stage, and the horizontal dotted lines correspond to the gas-phase ratios after the warm-up stage with the medium warm-up speed. In addition to the O-COM ratios (w.r.t. methanol) shown in Fig. 4, we also present a number of ratios between two O-COMs in Fig. 6. In the following subsections, we compare our observational results of each species to the "final" model with the "medium" warm-up speed in G22.

5.2.1. CH_3OCH_3 (DME) and CH_3OCHO (MF)

In the observations, DME and MF have the most stable column density ratios, and they have the best match with the G22 simulations (Fig. 4a,b). Their high abundances are often underproduced by experiments and simulations (Fedoseev et al. 2015; Chuang et al. 2016; Simons et al. 2020; Jin & Garrod 2020). However, the inclusion of the new formation routes in G22 enabled their models to reproduce our observational results on the gas-phase ratios of DME and MF with respect to methanol.

In the G22 models, more than 60% of the DME is formed in ices, through the reaction between methylene (CH_2) and methanol via

$$CH_2 + CH_3OH \rightarrow CH_3OCH_2, \text{ and} \quad (4)$$
$$H + CH_3OCH_2 \rightarrow CH_3OCH_3. \quad (5)$$

Nearly 90% of CH_3OCH_2 radicals are formed by the combination of CH_2 and CH_3O, in which CH_3O comes from the hydrogenation of formaldehyde (H_2CO) or H abstraction from methanol. As the reactant of two reactions, CH_2 directly affects the formation of DME ices. G22 set the activation energy barrier of the grain-surface reaction

$$C + H_2 \rightarrow CH_2 \quad (6)$$

to zero (Krasnokutski et al. 2016; Henning & Krasnokutski 2019) and added about 20 grain-surface CH_2-related reactions to the network (see Table 4 in G22). This greatly enhances the efficiency of forming CH_2 and its subsequent contribution to COMs formation. Nevertheless, this assumption is not fully supported by the combined experimental and theoretical work of Lamberts et al. (2022), who argued that the reaction between C and H_2 is unlikely to be fully barrierless on water ices. However, the effects to the full kinetic model may not be significant with a modest non-zero barrier of reaction (6). G22 also introduced a set of methylidyne (CH) reactions (Table 5 in G22) that can form CH_2 and larger hydrocarbons barrierlessly. These reactions can make up the CH_2 formation when reaction (6) has a barrier. According to G22, the inclusion of CH and CH_2 chemistry in the solid phase enhances the abundance of solid-phase DME by more than a factor of two. This emphasizes the importance of including the carbon hydrogenation to the chemical network (Qasim et al. 2020).

Besides the bottom-up formation of DME from CH_2, the photodissociation of CH_4 may also provide important ingredients. Several experimental studies have been able to produce DME from UV-irradiated ices of CH_3OH and CH_4 (Öberg et al. 2009; Paardekooper et al. 2016; Yocum et al. 2021). However, Fedoseev et al. (2015) and Chuang et al. (2016, 2017) did not observe DME formation in their experiments with CH_4 or H_2CO not included in the deposition, even when UV was introduced in Chuang et al. (2017).

According to G22, the remaining 40% DME is formed in the gas phase through two reactions:

$$CH_3OH + CH_3OH_2^+ \rightarrow CH_3OCH_4^+ + H_2O, \text{ and} \quad (7)$$
$$CH_3OCH_4^+ + NH_3 \rightarrow CH_3OCH_3 + NH_4^+. \quad (8)$$

In the first step, protonated DME is formed via the reaction between methanol and protonated methanol. The second step is the proton transfer to ammonia (Charnley et al. 1995; Rodgers & Charnley 2001; Taquet et al. 2016), where ammonia comes from ice sublimation, and therefore the reaction sequence would not be efficient under cold conditions (Skouteris et al. 2019).

In the solid phase, MF forms on grain surfaces mainly through the non-diffusive reaction (Chuang et al. 2016)

$$HCO + CH_3O \rightarrow CH_3OCHO. \quad (9)$$

A small contribution is made by the newly introduced three-body excited formation (3-BEF) reactions in the bulk ice

$$CH_3O + CO \rightarrow CH_3OCO, \quad (10)$$

whereby the hydrogenation of H_2CO would produce excited CH_3O that can overcome the reaction barrier (Jin & Garrod 2020). The CH_3OCO radicals can then recombine with H atoms to form MF. Reactions (9) and (10) occur in the cold collapse stage and contribute about 70% of the total MF. In the gas phase, the newly added reaction (Balucani et al. 2015)

$$O + CH_3OCH_2 \rightarrow CH_3OCHO + H \quad (11)$$

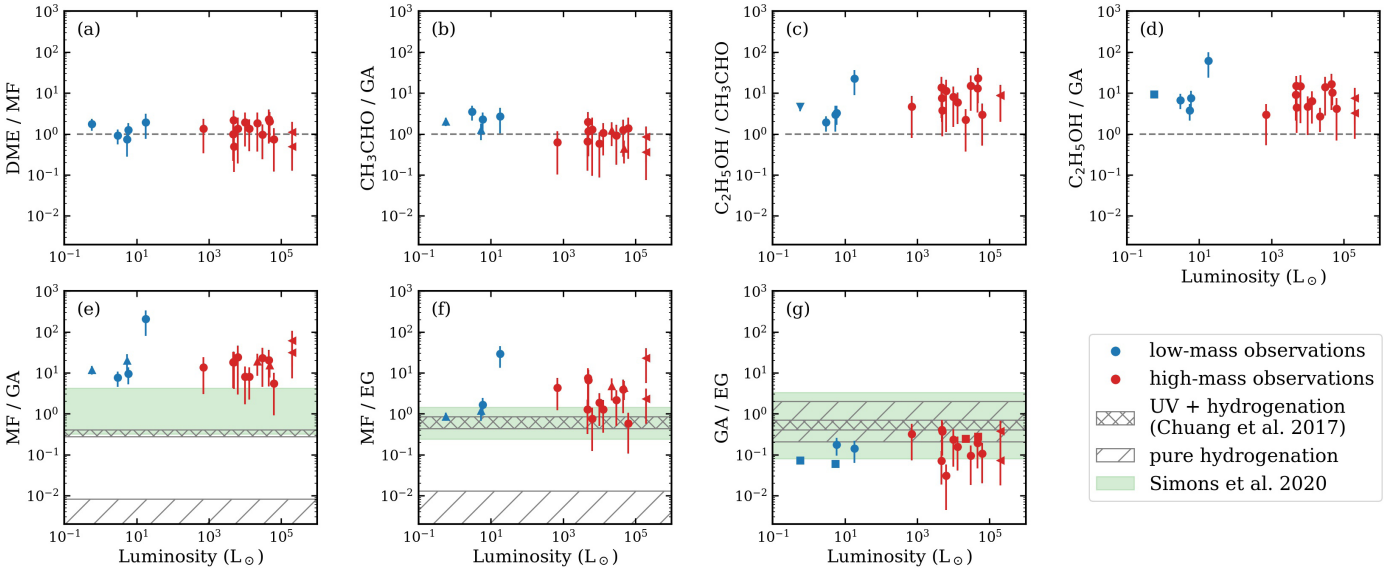

Fig. 6. Observed abundance ratios between seven pairs of O-COMs. Data points in blue and red correspond to the five low-mass sources from the literature and the 14 high-mass sources from the CoCCoA survey presented in this work, respectively (the same as Fig. 4). If the column densities of one species in the pair are upper limits, the ratios would be upper (lower) limits, and the data points are then shown as downward (upward) triangles instead of circles. Square data points without error bars indicate that the column densities of both species in the pair are upper limits. Dashed lines in panels a–d indicate a ratio of one. In panels e–g, the gray shaded areas with slashes or crosses indicate the ranges of the experimental results in Chuang et al. (2017), and the green shaded areas indicate the simulation predictions by Simons et al. (2020).

becomes the main production route when $T > 100$ K. The gaseous CH_3OCH_2 radicals can be released from ice mantles or converted from DME by OH abstraction (Shannon et al. 2014):

$$CH_3OCH_3 + OH \rightarrow CH_3OCH_2 + H_2O. \quad (12)$$

The formation of both DME and MF is strongly related to methanol and its precursor CH_3O. Simulations with different input n(H)/n(CO) ratios by Simons et al. (2020) and experiments by Santos et al. (2022) proposed that the final step of methanol formation is dominated by

$$CH_3O + H_2CO \rightarrow CH_3OH + HCO. \quad (13)$$

Chuang et al. (2016) noticed that H_2CO is a prerequisite for the formation of MF. In other words, without the input of H_2CO, there would be no MF detected in the outcome, which was also the case in Fedoseev et al. (2015), where only H and CO were used. Since CH_3O is necessary to form MF, it is inferred that the H abstraction from CH_3OH yields primarily CH_2OH, while CH_3O mainly comes from the hydrogenation of H_2CO. This may explain why DME and MF can retain relatively stable abundance ratios with respect to methanol among a large sample of sources, since the formation of all the three species tends to be strongly related with the same precursor, CH_3O. However, it is not clear whether the DME/MF ratio ∼1 (Fig. 6a) is a pure coincidence or there is some chemical balance between the two COMs.

5.2.2. C_2H_5OH

The observed abundance ratio of ethanol is on average one order of magnitude lower than the simulation results in G22. The scatter is also relatively large compared to DME and MF. The G22 models give nearly the same abundance after the collapse stage and the warm-up stage. This is because, in their models, ethanol is formed almost entirely in the early cold collapse stage on dust grains. The dominant reactions are:

$$C_2H_5 + OH \rightarrow C_2H_5OH \quad (14)$$

in the bulk ice and

$$CH_2 + CH_3OH \rightarrow C_2H_5OH \quad (15)$$

on the surface. The C_2H_5 radicals in reaction (14) are formed by diffusive reactions of atomic H with ethane (C_2H_6) and ethylene (C_2H_4). These routes may be supported by the experiments in Chuang et al. (2020) showing that ethanol can be formed through non-energetic processing of C_2H_2 ices. However, the efficiency of these reactions is not well constrained.

The OH radicals in reaction (14) come from photodissociation of water ice by external UV radiation. The G22 models used the same initial visual extinction ($A_{V,\,\mathrm{init}} = 3$) throughout the molecular cloud, while in reality, A_V is higher in the inner part of the cloud. This difference may result in an overestimation of the UV intensity in the cold collapse stage and hence the overproduction of ethanol on dust grains.

Apart from the production routes, there is also a recently proposed gas-phase destruction mechanism, the "ethanol tree" network (Skouteris et al. 2018), that is not included in the G22 models. This new network starts with the H abstraction from ethanol by halogen atoms or OH radicals, leading to two reactive radicals: CH_3CHOH and CH_2CH_2OH. These radicals are further converted into formic acid (HCOOH) and formaldehyde (H_2CO) by reacting with O atoms, along with other minor products (see branching ratios in Fig. 1 of Skouteris et al. 2018). As a result, the abundance of gas-phase ethanol decreases over time. Skouteris et al. (2018) predicts the ethanol/GA ratio to fall from ∼200 to ∼10 in about 1000 years. In our observations, the C_2H_5OH/GA ratios are around ten (see Fig. 6d). This suggests that the gas-phase destruction of ethanol in a later stage may play a role in explaining its overproduction in chemical models.

5.2.3. CH_3CHO

In the G22 simulations, the abundance ratio of CH_3CHO with respect to methanol in the solid phase after the collapse stage agrees well with our observational data. However, there are discrepancies among the warm-up stages with different timescales. The longer the warm-up stage is, the more CH_3CHO is produced, indicating substantial gas-phase formation. In the G22 models, only 25% of the total amount of CH_3CHO is formed in ices during the cold collapse stage ($T \sim 10$ K) through the hydrogenation of ketene

$$CH_2CO + 2H \rightarrow CH_3CHO. \quad (16)$$

About 35% is produced in the early warm-up stage ($T < 100$ K) by

$$CH_2 + H_2CO \rightarrow CH_3CHO \quad (17)$$

on the grain surface and

$$CH_3 + CO + H \rightarrow CH_3CHO \quad (18)$$

in the bulk ice. Nearly 40% is formed in the gas phase through the reaction

$$C_2H_5 + O \rightarrow CH_3CHO + H \quad (19)$$

after the desorption from dust grains at $T > 200$ K in the warm-up stage. Vazart et al. (2020) give a brief overview on the recorded gas-phase formation routes of CH_3CHO and explore some new reactions by theoretical computations. They confirm that reaction (19) is efficient in the temperature range of 7–300 K.

The observed ratios of CH_3CHO only match the modeled values after the cold collapse stage and the fast warm-up stage (the latter of which is not shown in Fig. 4d), which implies that the formation of CH_3CHO in the early stage may be more dominant than suggested by the G22 models. The experimental studies by Fedoseev et al. (2022) proposed a similar formation route for CH_3CHO, that is, the hydrogenation of ketene on cold (10 K) surfaces of mixed C, H, CO, and H_2O ices. They proposed that H_2CCO can be formed through hydrogenation of CCO radicals, which are the product of the barrierless association reaction between CO molecules and C atoms. Unfortunately, the intermediate products, CCO and HCCO, are very difficult to observe in experiments due to their high reactivity, and the relevant reaction rates remain undetermined. Chuang et al. (2020, 2021) also proposed formation routes from C_2H_2 ices to CH_3CHO at $T = 10$ K under both non-energetic and energetic conditions. To better understand the difference between the chemical modeling results in G22 (especially the gas-phase ratios after the warm-up stage) and our observational results, more knowledge about the relative importance of CH_3CHO formation in the solid and gas phase is needed.

We find it interesting to note the relation between CH_3CHO and the two more hydrogenated O-COMs, GA and C_2H_5OH. The ratios of CH_3CHO/GA and C_2H_5OH/CH_3CHO shown in Figs. 6b and c behave differently: CH_3CHO/GA is ∼1 with a small scatter comparable to DMF/MF, while C_2H_5OH/CH_3CHO exhibits a larger scatter. These results are counterintuitive since C_2H_5OH is suggested to be a direct hydrogenation product of CH_3CHO (e.g., experiments by Fedoseev et al. 2022), while GA and CH_3CHO are not usually simultaneously present in experiments. More investigation is needed to verify if GA and CH_3CHO are chemically linked.

5.2.4. CH_2OHCHO (GA) and $(CH_2OH)_2$ (EG)

In contrast to MF, simulations and experiments usually produce more GA than observations (e.g., Chuang et al. 2016, 2017; Simons et al. 2020), and the same occurs with the G22 models. Fedoseev et al. (2015, 2017) have confirmed experimentally that GA and EG can be formed in the solid phase through surface hydrogenation of CO molecules at $T = 13$ K. They suggest that GA and EG are the outcome of successive hydrogenation of glyoxal (HC(O)CHO), which is formed from two HCO radicals. In the G22 models, EG is mainly formed through the addition of two CH_2OH radicals in the solid phase:

$$CH_2OH + CH_2OH \rightarrow (CH_2OH)_2. \quad (20)$$

Most of the GA is formed through repetitive H abstraction from EG:

$$H + (CH_2OH)_2 \rightarrow CH_2OH_2CH_2O + H_2, \text{ and} \quad (21)$$
$$H + CH_2OHCH_2O \rightarrow CH_2OHCHO + H_2. \quad (22)$$

About 60% of the conversion from EG to GA through reaction (21)-(22) is finished in the cold collapse stage when $T \lesssim 10$ K, while about 30% occurs in the middle of the warm-up stage when $T \sim$ 100–200 K. A small portion of solid-phase GA is formed via the route proposed by Chuang et al. (2016):

$$CH_2OH + HCO \rightarrow CH_2OHCHO. \quad (23)$$

Despite the large scatter in the observed abundance ratios of GA and EG, it is obvious that EG is overall more abundant than GA in observations. However, the G22 models give the opposite result. This implies that the interconversion between EG and GA may not be well modeled in G22.

Another simulation work by Simons et al. (2020) computed their O-COM network with four H/CO input ratios (5–60%) at six low temperatures (8–20 K). They summarized the flux distribution of the network for the fiducial model with n(CO) = 10.0 cm $^{-3}$, n(H) = 2.5 cm $^{-3}$, and $T = 10$ K (see Fig. 8 of Simons et al. 2020). They found that the hydrogenation of glyoxal is more important to the GA formation than the H abstraction from EG. Their results also show that the relative abundance of GA to EG is very sensitive to the n(H)/n(CO) ratio. The observed abundance ratios of GA over EG are ∼0.1–1 (Fig. 6g), which corresponds to $n_{\rm initial}$(H)/$n_{\rm initial}$(CO) > 0.25 in their models. Chuang et al. (2017) were able to reproduce a similar GA/EG ratio through the hydrogenation of ices with CO:CH_3OH = 4:1 at $T = 14$ K and found it to be subject to the initial composition ratios. Besides pure hydrogenation, they tried introducing UV radiation, but the GA/EG ratio was not affected. The simulations and experiments mentioned above suggest that the formation of GA and EG is strongly regulated by the relative abundance of H atoms with respect to other ingredients such as CO. Parameters such as activation energy barriers and branching ratios of the related reactions of GA and EG formation may also attribute to the difference between simulations and observations.

The abundance ratio of GA with respect to methanol predicted by the G22 models is nearly one order of magnitude higher than our observational results. A possible reason for the overproduction by the chemical models is that GA has a higher desorption temperature than methanol (see Fig. 2 in Fedoseev et al. 2015). As a result, GA is expected to desorb and emit from a smaller region than methanol (for quantification, see the toy model described in Appendix B of Nazari et al. 2021). If our spatial resolution is not high enough to resolve the actual emitting

region of GA (suggested by the moment 0 map in Fig. A.1), there will be a beam dilution effect leading to an underestimated column density ratio of GA compared to the actual abundance ratio. An interesting fact is that EG has an even higher desorption temperature than GA (Fedoseev et al. 2015) and is expected to suffer more from beam dilution, but it is not overproduced by the G22 models. This means that if beam dilution actually accounts for the underestimation of GA in observations, EG would have been underproduced by the G22 models; otherwise, there should be other reasons for the observed GA depletion.

5.3. The influence of energetic processes

As mentioned in Sect. 5.2.4, Chuang et al. (2017) showed that the ratios among MF, GA, and EG can be altered by UV radiation. The ratios of MF with respect to GA and EG both increase by nearly two orders of magnitude when introducing UV radiation to the experiments, while the ratio between GA and EG is not much affected. The second row of Fig. 6 shows a comparison between observations, simulations, and experiments (this work, Simons et al. 2020; Chuang et al. 2017, respectively). The UV intensity was not varied during the experiments, but the discrepancy between pure hydrogenation and UV irradiation implies a positive correlation between the UV irradiation and the relative abundance of MF. However, the observed ratios of MF/GA and MF/EG are still higher overall than the values produced by simulations and experiments.

In G22, one of the models tests the influence of cosmic ray-induced ionization and UV-induced photodissociation, which shows an obvious enhancement of the O-COM abundances. The "final" model includes these energetic processes but with a fixed efficiency, as do the simulations in Simons et al. (2020). The G22 models are able to reproduce enough MF by introducing a new set of non-diffusive reactions, but the abundances of GA and EG are not very consistent with our observations. Experiments by Öberg et al. (2009) suggest that the final product composition after irradiating CH_3OH ices with UV lamps depends more on the UV fluence and temperature than the UV flux itself. There is a possible explanation that the short timescale offsets the high UV flux in high-mass sources, and the total UV fluence falls in the same order as low-mass sources. To figure out the influence of energetic processes on COM chemistry, especially in the solid phase, more experiments and simulations with varied parameters are needed. Observations of larger samples of protostellar objects with different masses and luminosities are also needed in order to provide more reliable statistics of COMs ratios.

5.4. O-COMs from clouds to comets

Figure 7 summarizes the observed O-COM ratios with respect to methanol in different astronomical objects. The data of protostars are represented by the average ratios of the low-mass and high-mass sources discussed in this work, and the uncertainties correspond to the standard deviation. In the figure, we compare the statistical data in this work with the literature data of the outbursting protostar V883(FU) Ori (Lee et al. 2019b) and the protoplanetary disk around Oph IRS 48 (Brunken et al. 2022). Two comets, 67P/Churyumov–Gerasimenko (67P/C–G) (Rubin et al. 2019; Drozdovskaya et al. 2019) and 46P/Wirtanen (Biver et al. 2021), are also taken into account, as they reflect the pristine chemical composition in our solar system. All the sources except the two comets were observed by ALMA. The data of 67P/C-G were collected by the Rosetta Orbiter Spectrometer for Ion and Neutral Analysis (ROSINA), and the data of 46P/Wirtanen were

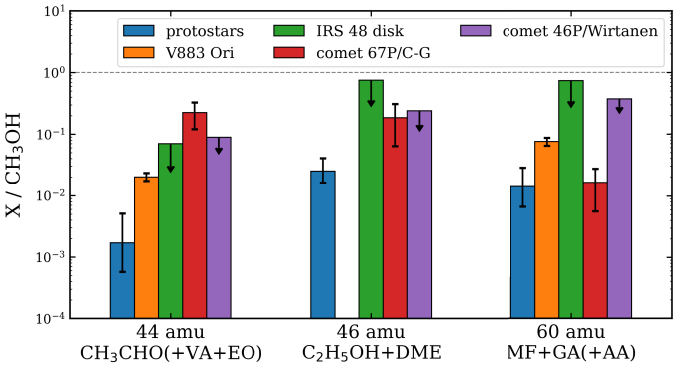

Fig. 7. Column density ratios of selected O-COMs with respect to methanol in different astronomical objects (see references in Sect. 5.4). Species are divided into three groups with different atomic mass units (amu); those in parentheses are only shown for the degenerate detections in the comet 67P/C-G by the ROSINA mass spectrometer, and they have not been detected separately in other sources. The column densities of the species with the same atomic mass units have been added together. The data of IRS 48 are shown as upper limits due to the possible underestimation of the column density of methanol.

taken by the Institut de Radio Astronomie Millimétrique (IRAM) 30-m telescope and the NOrthern Extended Millimeter Array (NOEMA). ROSINA is a mass spectrometer, and it cannot distinguish among isomers with the same mass (e.g., C_2H_5OH and DME have the same atomic mass unit of 46). Considering the data availability, we chose three groups of O-COMs for comparison:

amu = 44: CH_3CHO, CH_2CHOH (vinyl alcohol, VA), c-C_2H_4O (ethylene oxide, EO);

amu = 46: C_2H_5OH, DME; and

amu = 60: MF, GA, CH_3COOH (acetic acid, AA).

We mention EO, VA, and AA only for the potential degeneracy of the detection of 67P/C-G; they were not searched for nor detected in other sources except one low-mass protostellar object (IRAS 16293-2242 B) that we consider here. The O-COM ratios of IRS 48 may be overestimated since the column density of methanol was determined from lines that are likely to be optically thick (hence upper limit signs are used).

In general, protostellar sources have lower O-COM ratios than other sources, especially for the group of amu = 44. For the other two groups, considering that the data of IRS 48 may be overestimated, the O-COM ratios are more comparable among the samples. However, the sample here is too small to draw any robust conclusion. A larger sample of sources at different evolutionary stages are needed to study the chemical inheritance throughout star formation.

5.5. JWST ice observations

With JWST successfully operating, it is now becoming more possible to detect COMs other than methanol in ices. The absorption features for the identification of O-COM ices are mainly located in the mid-infrared between 2 and 15 μm (Boogert et al. 2015; Rocha et al. 2022). The absorption features at 7.24 and 7.41 μm observed by ISO (Schutte et al. 1999), *Spitzer*/IRS (Öberg et al. 2011), and the latest JWST/MIRI (Yang et al. 2022; McClure et al. 2023) are tentatively attributed to CH_3CHO and C_2H_5OH ices. Additionally, the feature around

11.3 μm in the JWST spectra may also have some contributions from CH_3CHO, C_2H_5OH, and MF (Terwisscha van Scheltinga et al. 2018, 2021). However, more detailed spectral modeling is needed to confirm the detection of these COMs. Once JWST observations with larger samples and higher sensitivities are available, we will be able to estimate the ratios of CH_3CHO and C_2H_5OH with respect to methanol in ices based on the absorption features at 7.2 and 7.4 μm. By comparing their ice ratios to the gas-phase ones in the same sources, we can get an idea as to whether and to what extent these species participate in gas-phase chemistry after they sublimate from the ice mantles of dust grains.

6. Conclusions

We analyzed the spectra of 14 high-mass protostellar objects from the CoCCoA survey. We focused on six selected O-COMs: CH_3CHO, C_2H_5OH, DME, MF, GA, and EG, and we derived their column densities as well as the excitation temperatures for the 14 sources. We also performed various comparisons between the observed O-COM ratios with respect to methanol and the results from previous simulations and experiments. We summarize our conclusions as follows:

1. The gas-phase column density ratios of the six selected O-COMs with respect to methanol show no clear difference between the five low-mass objects studied previously and the 14 high-mass protostellar objects observed with ALMA, suggesting that these species are mainly formed under similar conditions. Current astrochemical simulations and experiments support the possibility of early formation of COM ices on dust grains in the pre-stellar stage, before the environments in low- and high-mass star-forming regions begin to diverge. However, the possibility exists that other gas-phase formation routes also play an important role in shaping the COM ratios, which needs more investigations to pin down;
2. DME and MF show smaller scatter in their ratios with respect to methanol than CH_3CHO, C_2H_5OH, GA, and EG. This may hint at some chemical links among DME, MF, and methanol, such as having the same precursor (e.g., CH_3O) in their formation routes;
3. The ratios among pairs of O-COMs also show the same trends between the low-mass and the high-mass groups. In particular, the ratios of DME/MF and CH_3CHO/GA are quite consistently around one, while others show larger scatter;
4. Previous experiments show that the ratios of MF/GA and MF/EG can be significantly enhanced by UV irradiation, but the observed values are even higher than the laboratory ones. The ratio of GA/EG is not affected by UV in experiments and match well with our observations;
5. The comparison of our observational data with the state-of-the-art models shows consistency in the O-COM ratios for some species, such as DME and MF. The differences between models and observations may result from less constrained gas-phase chemistry (CH_3CHO and C_2H_5OH) and the different emitting areas under limited spatial resolutions (GA and EG). Further chemical simulations and laboratory experiments are important to testing and exploring possible explanations;
6. The comparison of O-COM ratios among sources at different evolutionary stages may probe the chemical inheritance during star formation processes. However, observations toward larger samples are needed to enable statistical analyses.

ALMA line surveys toward large samples of star-forming regions are shedding light on the origin of COMs and the chemical evolution in the early stages of star formation. We look forward to linking our results to more ALMA observations on gas-phase COMs as well as to the upcoming JWST mid-infrared data on solid-phase COMs in order to probe their formation history.

Acknowledgements. The authors are grateful to the entire CoCCoA team for their interest in this study. This paper makes use of the following ALMA data: ADS/JAO.ALMA#2019.1.00246.S. ALMA is a partnership of ESO (representing its member states), NSF (USA) and NINS (Japan), together with NRC (Canada), MOST and ASIAA (Taiwan), and KASI (Republic of Korea), in cooperation with the Republic of Chile. The Joint ALMA Observatory is operated by ESO, AUI/NRAO, and NAOJ. Astrochemistry in Leiden is supported by the Netherlands Research School for Astronomy (NOVA), by funding from the European Research Council (ERC) under the European Union's Horizon 2020 research and innovation programme (grant agreement No. 101019751 MOLDISK), by the Dutch Research Council (NWO) grants TOP-1 614.001.751 and 618.000.001, and by the Danish National Research Foundation through the Center of Excellence "InterCat" (Grant agreement no.: DNRF150). The National Radio Astronomy Observatory is a facility of the National Science Foundation operated under cooperative agreement by Associated Universities, Inc. Y.C. acknowledges Jiao He for useful discussion about astrochemical experiments. J.K.J. acknowledges support from the Independent Research Fund Denmark (grant number 0135-00123B). M.N.D. is supported by the Swiss National Science Foundation (SNSF) Ambizione grant 180079, the Center for Space and Habitability (CSH) Fellowship, and the IAU Gruber Foundation Fellowship. S.I. acknowledges the Danish National Research Foundation through the Center of Excellence "InterCat" (Grant agreement no.: DNRF150). B.M.K. is supported by the Swiss National Science Foundation (SNSF) Ambizione grant 180079. N.F.W.L. acknowledges funding by the Swiss National Science Foundation Ambizione grant 193453.

References

Bacmann, A., Taquet, V., Faure, A., Kahane, C., & Ceccarelli, C. 2012, A&A, 541, A12
Balucani, N., Ceccarelli, C., & Taquet, V. 2015, MNRAS, 449, L16
Belloche, A., Müller, H. S. P., Garrod, R. T., & Menten, K. M. 2016, A&A, 587, A91
Belloche, A., Maury, A. J., Maret, S., et al. 2020, A&A, 635, A198
Beltrán, M. T., Codella, C., Viti, S., Neri, R., & Cesaroni, R. 2009, ApJ, 690, L93
Beltrán, M. T., Sánchez-Monge, Á., Cesaroni, R., et al. 2014, A&A, 571, A52
Beltrán, M. T., Cesaroni, R., Rivilla, V. M., et al. 2018, A&A, 615, A141
Bianchi, E., Chandler, C. J., Ceccarelli, C., et al. 2020, MNRAS, 498, L87
Bisschop, S. E., Jørgensen, J. K., van Dishoeck, E. F., & de Wachter, E. B. M. 2007, A&A, 465, 913
Biver, N., Bockelée-Morvan, D., Boissier, J., et al. 2021, A&A, 648, A49
Blake, G. A., Sutton, E. C., Masson, C. R., & Phillips, T. G. 1987, ApJ, 315, 621
Boogert, A. C. A., Gerakines, P. A., & Whittet, D. C. B. 2015, ARA&A, 53, 541
Bottinelli, S., Ceccarelli, C., Lefloch, B., et al. 2004, ApJ, 615, 354
Brogan, C. L., Hunter, T. R., & Fomalont, E. B. 2018, ArXiv e-prints, [arXiv:1805.05266]
Brunken, N. G. C., Booth, A. S., Leemker, M., et al. 2022, A&A, 659, A29
Caselli, P., & Ceccarelli, C. 2012, A&ARv, 20, 56
Cazaux, S., Tielens, A. G. G. M., Ceccarelli, C., et al. 2003, ApJ, 593, L51
Ceccarelli, C., Codella, C., Balucani, N., et al. 2022, ArXiv e-prints, [arXiv:2206.13270]
Charnley, S. B., Kress, M. E., Tielens, A. G. G. M., & Millar, T. J. 1995, ApJ, 448, 232
Chibueze, J. O., Omodaka, T., Handa, T., et al. 2014, ApJ, 784, 114
Chuang, K. J., Fedoseev, G., Ioppolo, S., van Dishoeck, E. F., & Linnartz, H. 2016, MNRAS, 455, 1702
Chuang, K. J., Fedoseev, G., Qasim, D., et al. 2017, MNRAS, 467, 2552
Chuang, K. J., Fedoseev, G., Qasim, D., et al. 2020, A&A, 635, A199
Chuang, K. J., Fedoseev, G., Scirè, C., et al. 2021, A&A, 650, A85
Codella, C., López-Sepulcre, A., Ohashi, S., et al. 2022, MNRAS, 515, 543
Coletta, A., Fontani, F., Rivilla, V. M., et al. 2020, A&A, 641, A54
Colzi, L., Rivilla, V. M., Beltrán, M. T., et al. 2021, A&A, 653, A129
Csengeri, T., Belloche, A., Bontemps, S., et al. 2019, A&A, 632, A57
Csengeri, T., Wyrowski, F., Menten, K. M., et al. 2022, A&A, 658, A193
Cummins, S. E., Linke, R. A., & Thaddeus, P. 1986, ApJS, 60, 819
Cuppen, H. M., van Dishoeck, E. F., Herbst, E., & Tielens, A. G. G. M. 2009, A&A, 508, 275

Cyganowski, C. J., Brogan, C. L., Hunter, T. R., Churchwell, E., & Zhang, Q. 2011, ApJ, 729, 124
De Simone, M., Ceccarelli, C., Codella, C., et al. 2020, ApJ, 896, L3
Drozdovskaya, M. N., van Dishoeck, E. F., Rubin, M., Jørgensen, J. K., & Altwegg, K. 2019, MNRAS, 490, 50
El-Abd, S. J., Brogan, C. L., Hunter, T. R., et al. 2019, ApJ, 883, 129
Endres, C. P., Schlemmer, S., Schilke, P., Stutzki, J., & Müller, H. S. P. 2016, J. Mol. Spectrosc., 327, 95
Faúndez, S., Bronfman, L., Garay, G., et al. 2004, A&A, 426, 97
Fedoseev, G., Cuppen, H. M., Ioppolo, S., Lamberts, T., & Linnartz, H. 2015, MNRAS, 448, 1288
Fedoseev, G., Chuang, K. J., Ioppolo, S., et al. 2017, ApJ, 842, 52
Fedoseev, G., Qasim, D., Chuang, K.-J., et al. 2022, ApJ, 924, 110
Fuchs, G. W., Cuppen, H. M., Ioppolo, S., et al. 2009, A&A, 505, 629
Garrod, R. T., Jin, M., Matis, K. A., et al. 2022, ApJS, 259, 1
Ge, J. X., He, J. H., Chen, X., & Takahashi, S. 2014, MNRAS, 445, 1170
Gerakines, P., Yarnall, Y., & Hudson, R. 2022, in American Astronomical Society Meeting Abstracts, 54, 134.02
Gieser, C., Semenov, D., Beuther, H., et al. 2019, A&A, 631, A142
Henning, T. K., & Krasnokutski, S. A. 2019, Nat. Astron., 3, 568
Herbst, E., & van Dishoeck, E. F. 2009, ARA&A, 47, 427
Hiraoka, K., Miyagoshi, T., Takayama, T., Yamamoto, K., & Kihara, Y. 1998, ApJ, 498, 710
Hollis, J. M., Lovas, F. J., & Jewell, P. R. 2000, ApJ, 540, L107
Hollis, J. M., Lovas, F. J., Jewell, P. R., & Coudert, L. H. 2002, ApJ, 571, L59
Hsu, S.-Y., Liu, S.-Y., Liu, T., et al. 2022, ApJ, 927, 218
Hudson, R. L., & Ferrante, R. F. 2020, MNRAS, 492, 283
Hudson, R. L., & Gerakines, P. A. 2019, MNRAS, 482, 4009
Hudson, R. L., & Yarnall, Y. Y. 2022, Icarus, 377, 114899
Hudson, R. L., Gerakines, P. A., Yarnall, Y. Y., & Coones, R. T. 2021, Icarus, 354, 114033
Imai, M., Oya, Y., Svoboda, B., et al. 2022, ApJ, 934, 70
Isokoski, K., Bottinelli, S., & van Dishoeck, E. F. 2013, A&A, 554, A100
Issac, N., Tej, A., Liu, T., et al. 2020, MNRAS, 497, 5454
Jiménez-Serra, I., Vasyunin, A. I., Caselli, P., et al. 2016, ApJ, 830, L6
Jin, M., & Garrod, R. T. 2020, ApJS, 249, 26
Johnstone, D., Boonman, A. M. S., & van Dishoeck, E. F. 2003, A&A, 412, 157
Jørgensen, J. K., Bourke, T. L., Myers, P. C., et al. 2005, ApJ, 632, 973
Jørgensen, J. K., van der Wiel, M. H. D., Coutens, A., et al. 2016, A&A, 595, A117
Jørgensen, J. K., Müller, H. S. P., Calcutt, H., et al. 2018, A&A, 620, A170
Jørgensen, J. K., Belloche, A., & Garrod, R. T. 2020, ARA&A, 58, 727
König, C., Urquhart, J. S., Csengeri, T., et al. 2017, A&A, 599, A139
Krasnokutski, S. A., Kuhn, M., Renzler, M., et al. 2016, ApJ, 818, L31
Lamberts, T., Fedoseev, G., van Hemert, M. C., et al. 2022, ApJ, 928, 48
Lee, C.-F., Codella, C., Li, Z.-Y., & Liu, S.-Y. 2019a, ApJ, 876, 63
Lee, J.-E., Lee, S., Baek, G., et al. 2019b, Nat. Astron., 3, 314
Ligterink, N. F. W., Tenenbaum, E. D., & van Dishoeck, E. F. 2015, A&A, 576, A35
Ligterink, N. F. W., El-Abd, S. J., Brogan, C. L., et al. 2020, ApJ, 901, 37
Linnartz, H., Ioppolo, S., & Fedoseev, G. 2015, Int. Rev. Phys. Chem., 34, 205
Manigand, S., Jørgensen, J. K., Calcutt, H., et al. 2020, A&A, 635, A48
Maud, L. T., Moore, T. J. T., Lumsden, S. L., et al. 2015, MNRAS, 453, 645
Maury, A. J., Belloche, A., André, P., et al. 2014, A&A, 563, A2
McClure, M. K., Rocha, W. R. M., Pontoppidan, K. M., et al. 2023, Nat. Astron., 7, 431
McGuire, B. A. 2022, ApJS, 259, 30
Milam, S. N., Savage, C., Brewster, M. A., Ziurys, L. M., & Wyckoff, S. 2005, ApJ, 634, 1126
Mininni, C., Beltrán, M. T., Rivilla, V. M., et al. 2020, A&A, 644, A84
Müller, H. S. P., Thorwirth, S., Roth, D. A., & Winnewisser, G. 2001, A&A, 370, L49
Müller, H. S. P., Schlöder, F., Stutzki, J., & Winnewisser, G. 2005, J. Mol. Struct., 742, 215
Nazari, P., van Gelder, M. L., van Dishoeck, E. F., et al. 2021, A&A, 650, A150
Nazari, P., Meijerhof, J. D., van Gelder, M. L., et al. 2022a, A&A, 668, A109
Nazari, P., Tabone, B., Rosotti, G. P., et al. 2022b, A&A, 663, A58
Nazari, P., Tabone, B., & Rosotti, G. P. 2023, A&A, 671, A107
Öberg, K. I., Garrod, R. T., van Dishoeck, E. F., & Linnartz, H. 2009, A&A, 504, 891
Öberg, K. I., Boogert, A. C. A., Pontoppidan, K. M., et al. 2011, ApJ, 740, 109
Öberg, K. I., Guzmán, V. V., Furuya, K., et al. 2015, Nature, 520, 198
Paardekooper, D. M., Bossa, J. B., & Linnartz, H. 2016, A&A, 592, A67
Pickett, H. M., Poynter, R. L., Cohen, E. A., et al. 1998, J. Quant. Spec. Radiat. Transf., 60, 883
Qasim, D., Fedoseev, G., Chuang, K. J., et al. 2020, Nat. Astron., 4, 781
Rachid, M. G., Terwisscha van Scheltinga, J., Koletzki, D., & Linnartz, H. 2020, A&A, 639, A4
Rachid, M. G., Brunken, N., de Boe, D., et al. 2021, A&A, 653, A116
Rachid, M. G., Rocha, W. R. M., & Linnartz, H. 2022, A&A, 665, A89
Rocha, W. R. M., Rachid, M. G., Olsthoorn, B., et al. 2022, A&A, 668, A63
Rodgers, S. D., & Charnley, S. B. 2001, MNRAS, 320, L61
Rubin, M., Altwegg, K., Balsiger, H., et al. 2019, MNRAS, 489, 594
Sánchez-Monge, Á., Cesaroni, R., Beltrán, M. T., et al. 2013, A&A, 552, A10
Sandell, G. 2000, A&A, 358, 242
Santos, J. C., Chuang, K.-J., Lamberts, T., et al. 2022, ApJ, 931, L33
Schilke, P., Groesbeck, T. D., Blake, G. A., Phillips, & T. G. 1997, ApJS, 108, 301
Schutte, W. A., Boogert, A. C. A., Tielens, A. G. G. M., et al. 1999, A&A, 343, 966
Scibelli, S., Shirley, Y., Vasyunin, A., & Launhardt, R. 2021, MNRAS, 504, 5754
Shalabiea, O. M., & Greenberg, J. M. 1994, A&A, 290, 266
Shannon, R. J., Caravan, R. L., Blitz, M. A., & Heard, D. E. 2014, Phys. Chem. Chem. Phys., 16, 3466
Simons, M. A. J., Lamberts, T., & Cuppen, H. M. 2020, A&A, 634, A52
Skouteris, D., Balucani, N., Ceccarelli, C., et al. 2018, ApJ, 854, 135
Skouteris, D., Balucani, N., Ceccarelli, C., et al. 2019, MNRAS, 482, 3567
Soma, T., Sakai, N., Watanabe, Y., & Yamamoto, S. 2018, ApJ, 854, 116
Tang, X. D., Henkel, C., Wyrowski, F., et al. 2018, A&A, 611, A6
Taquet, V., Wirström, E. S., & Charnley, S. B. 2016, ApJ, 821, 46
Terwisscha van Scheltinga, J., Ligterink, N. F. W., Boogert, A. C. A., van Dishoeck, E. F., & Linnartz, H. 2018, A&A, 611, A35
Terwisscha van Scheltinga, J., Marcandalli, G., McClure, M. K., Hogerheijde, M. R., & Linnartz, H. 2021, A&A, 651, A95
Towner, A. P. M., Brogan, C. L., Hunter, T. R., & Cyganowski, C. J. 2021, ApJ, 923, 263
van der Tak, F. F. S., van Dishoeck, E. F., Evans, Neal J., I., Bakker, E. J., & Blake, G. A. 1999, ApJ, 522, 991
van der Tak, F. F. S., van Dishoeck, E. F., Evans, Neal J., I., & Blake, G. A. 2000, ApJ, 537, 283
van der Tak, F. F. S., Chavarría, L., Herpin, F., et al. 2013, A&A, 554, A83
van Gelder, M. L., Tabone, B., Tychoniec, Ł., et al. 2020, A&A, 639, A87
van Gelder, M. L., Nazari, P., Tabone, B., et al. 2022, A&A, 662, A67
Vastel, C., Ceccarelli, C., Lefloch, B., & Bachiller, R. 2014, ApJ, 795, L2
Vastel, C., Bottinelli, S., Caux, E., Glorian, J. M., & Boiziot, M. 2015, in SF2A-2015: Proceedings of the Annual meeting of the French Society of Astronomy and Astrophysics, 313
Vazart, F., Ceccarelli, C., Balucani, N., Bianchi, E., & Skouteris, D. 2020, MNRAS, 499, 5547
Walsh, C., Loomis, R. A., Öberg, K. I., et al. 2016, ApJ, 823, L10
Watanabe, N., & Kouchi, A. 2002, ApJ, 571, L173
Widicus Weaver, S. L., Laas, J. C., Zou, L., et al. 2017, ApJS, 232, 3
Williams, G. M., Cyganowski, C. J., Brogan, C. L., et al. 2022, MNRAS, 509, 748
Wilson, T. L., & Rood, R. 1994, ARA&A, 32, 191
Wu, Y. W., Sato, M., Reid, M. J., et al. 2014, A&A, 566, A17
Yang, Y.-L., Sakai, N., Zhang, Y., et al. 2021, ApJ, 910, 20
Yang, Y.-L., Green, J. D., Pontoppidan, K. M., et al. 2022, ApJ, 941, L13
Yocum, K. M., Milam, S. N., Gerakines, P. A., & Widicus Weaver, S. L. 2021, ApJ, 913, 61
Zhang, B., Zheng, X. W., Reid, M. J., et al. 2009, ApJ, 693, 419

[1] Leiden Observatory, Leiden University, PO Box 9513, 2300 RA Leiden, The Netherlands
e-mail: ychen@strw.leidenuniv.nl
[2] National Radio Astronomy Observatory, 520 Edgemont Road, Charlottesville, VA 22903, USA
[3] Harvard-Smithsonian Center for Astrophysics, 60 Garden Street, Cambridge, MA 02138, USA
[4] Max Planck Institut für Extraterrestrische Physik (MPE), Giessenbachstrasse 1, 85748 Garching, Germany
[5] Laboratory for Astrophysics, Leiden Observatory, Leiden University, PO Box 9513, 2300 RA Leiden, The Netherlands
[6] Center for Star and Planet Formation, Niels Bohr Institute & Natural History Museum of Denmark, University of Copenhagen, Øster Voldgade 5-7, 1350 Copenhagen K, Denmark
[7] NASA Goddard Space Flight Center, Greenbelt, MD 20771, USA
[8] Division of Geological and Planetary Sciences, California Institute of Technology, Pasadena, CA 91125, USA

[9] Istituto Nazionale di Astrofisica (INAF), Osservatorio Astrofisico di Arcetri, Largo E. Fermi 5, 50125, Florence, Italy
[10] Université Grenoble Alpes, Centre national de la recherche scientifique (CNRS), Institut de Planétologie et d'Astrophysique de Grenoble (IPAG), 414 Rue de la Piscine, 38400 Saint-Martin-d'Hères, France
[11] Department of Chemistry, University of British Columbia, 2036 Main Mall, Vancouver BC V6T 1Z1, Canada
[12] Center for Space and Habitability, Universität Bern, Gesellschaftsstrasse 6, 3012 Bern, Switzerland
[13] Department of Chemistry, University of Virginia, Charlottesville, 409 McCormick Road, PO Box 400319, VA 22904, USA
[14] Department of Astronomy, University of Virginia, Charlottesville, 530 McCormick Road, PO Box 400325, VA 22904, USA
[15] Center for Interstellar Catalysis, Department of Physics and Astronomy, Aarhus University, Ny Munkegade 120, Aarhus C 8000, Denmark
[16] Astrochemistry Laboratory, Code 691, NASA Goddard Space Flight Center, Greenbelt, MD 20771, USA
[17] Department of Physics, Catholic University of America, 200 Hannan Hall, Washington, DC 20064, USA
[18] Physics Institute, Space Research and Planetary Sciences, University of Bern, Sidlerstrasse 5, 3012 Bern, Switzerland
[19] Department of Chemistry, Massachusetts Institute of Technology, 77 Massachusetts Ave., Cambridge, MA 02139, USA

Appendix A: Additional figures

Figure A.1 shows the moment 0 maps of selected O-COMs in G19.88-0.53. Figure A.2 shows how the fitting with the best fit and the upper and lower limits of T_{ex} appear, taking MF and G19.88-0.53 as an example. Figure A.3 shows the spectral fitting with two components, taking G19.01-0.03 as an example. Figure A.4 shows the ratios of the six selected O-COMs with respect to methanol, which is the same as Fig. 4 but with the intercept error in Eq. (1) included. Figure A.5 shows the full spectral fitting results of selected O-COMs for the representative source G19.88-0.53. Figures A.6-A.8 show the zoom-in fitting of each O-COM.

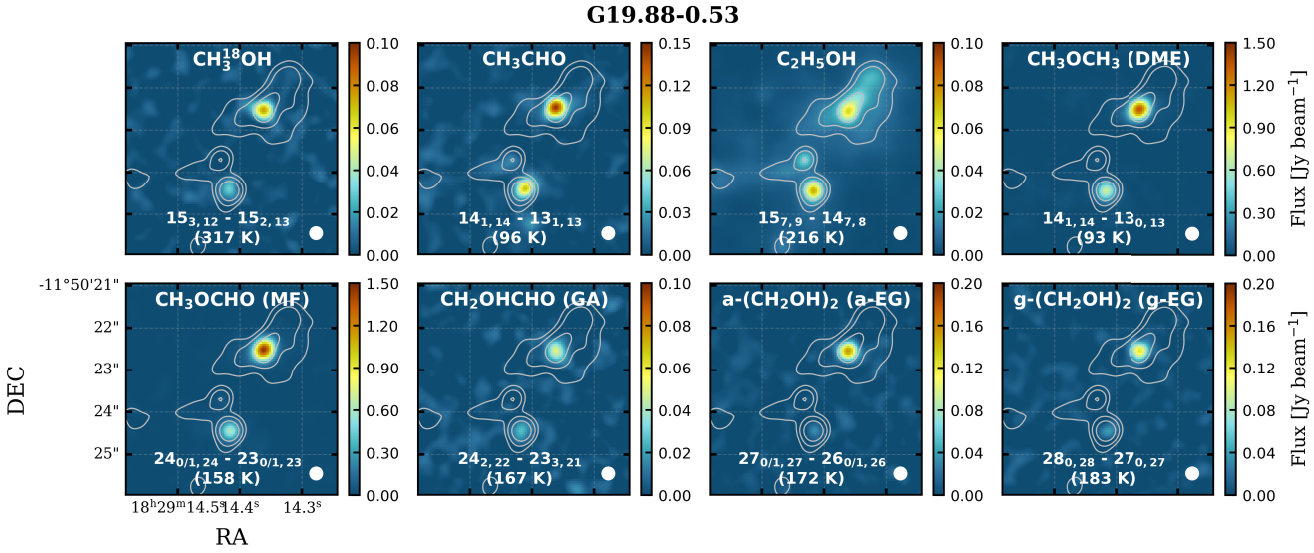

Fig. A.1: Moment 0 maps of selected O-COMs in the representative source G19.88-0.53. Contours and beams are the same as those in Fig. 1. We chose the strongest and unblended (or less blended) line in the upper tuning to make a moment 0 map of each species. The quantum numbers and the upper energy level are indicated in white bold text at the bottom of each panel. The images are integrated over the FWHM with respect to the line center.

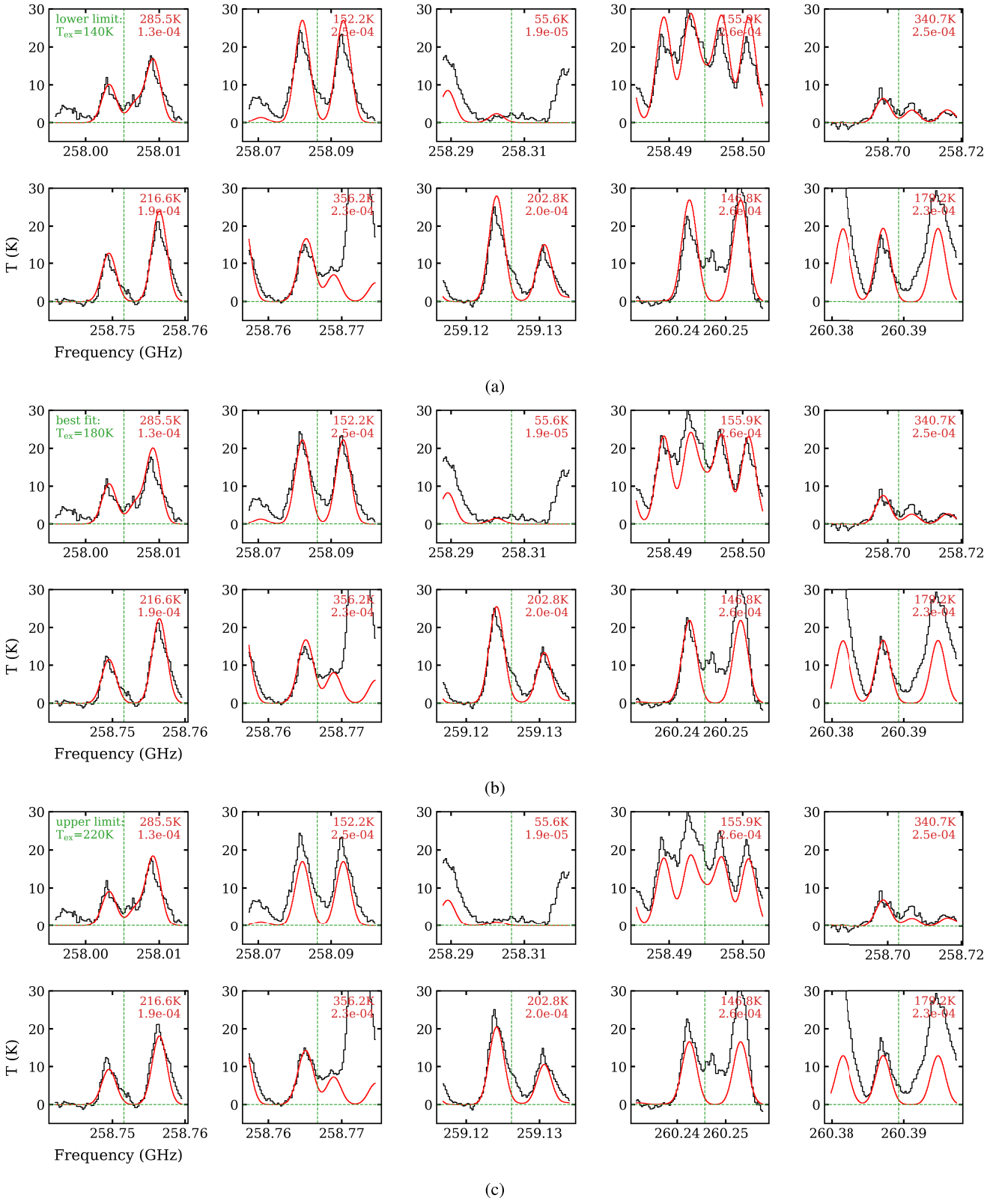

Fig. A.2: Example of spectral fitting with (a) the lower limit, (b) the best fit, and (c) the upper limit of the excitation temperature (T_{ex}) of MF (CH_3OCHO) in the spectrum of G19.88-0.53. Ten transitions with different upper energy levels (E_{up}) are shown for comparison.

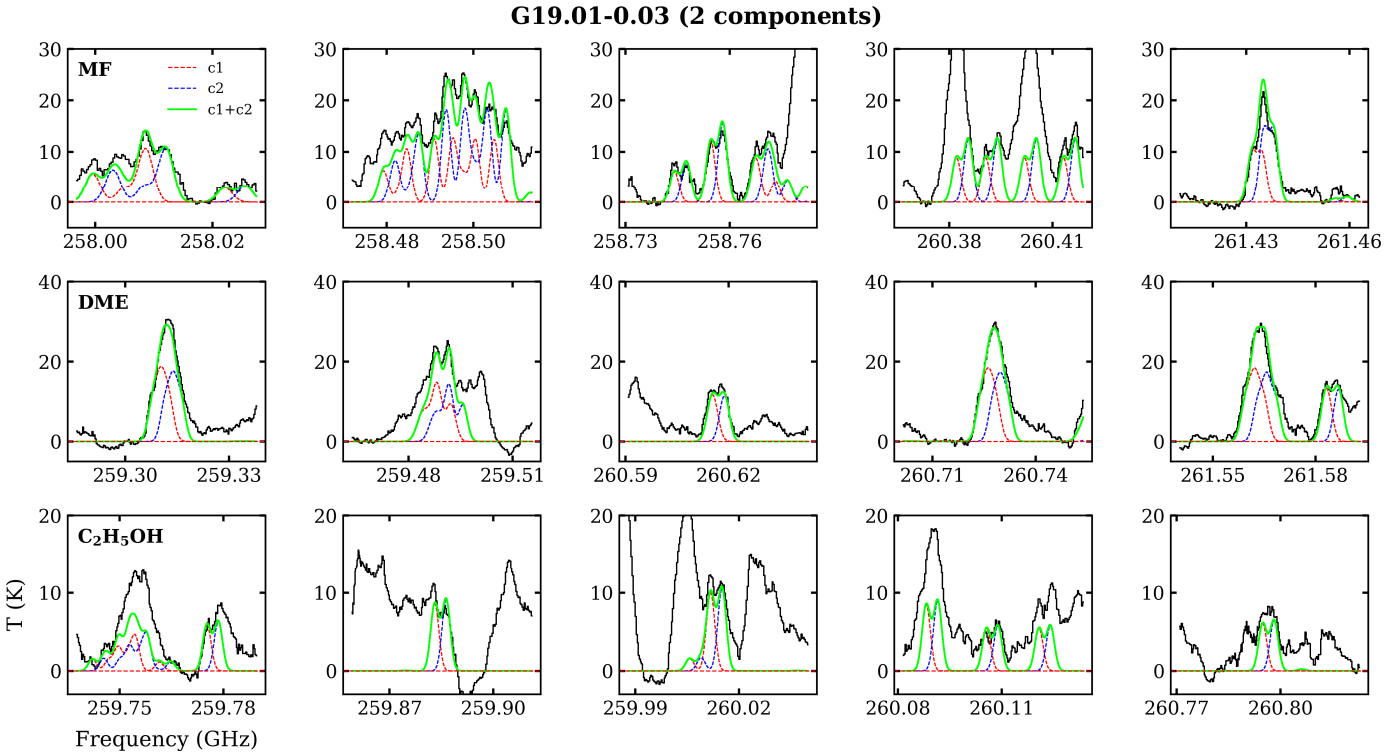

Fig. A.3: Example of spectral fitting that introduces two components, represented by three O-COMs of G19.01-0.03. The observed spectrum is shown in solid black. The two components (c1 and c2) are shown with dashed red and blue lines, respectively. The sum of the two components is shown in solid green. See Tables B.1–B.4 for other sources and species that are fit by two components.

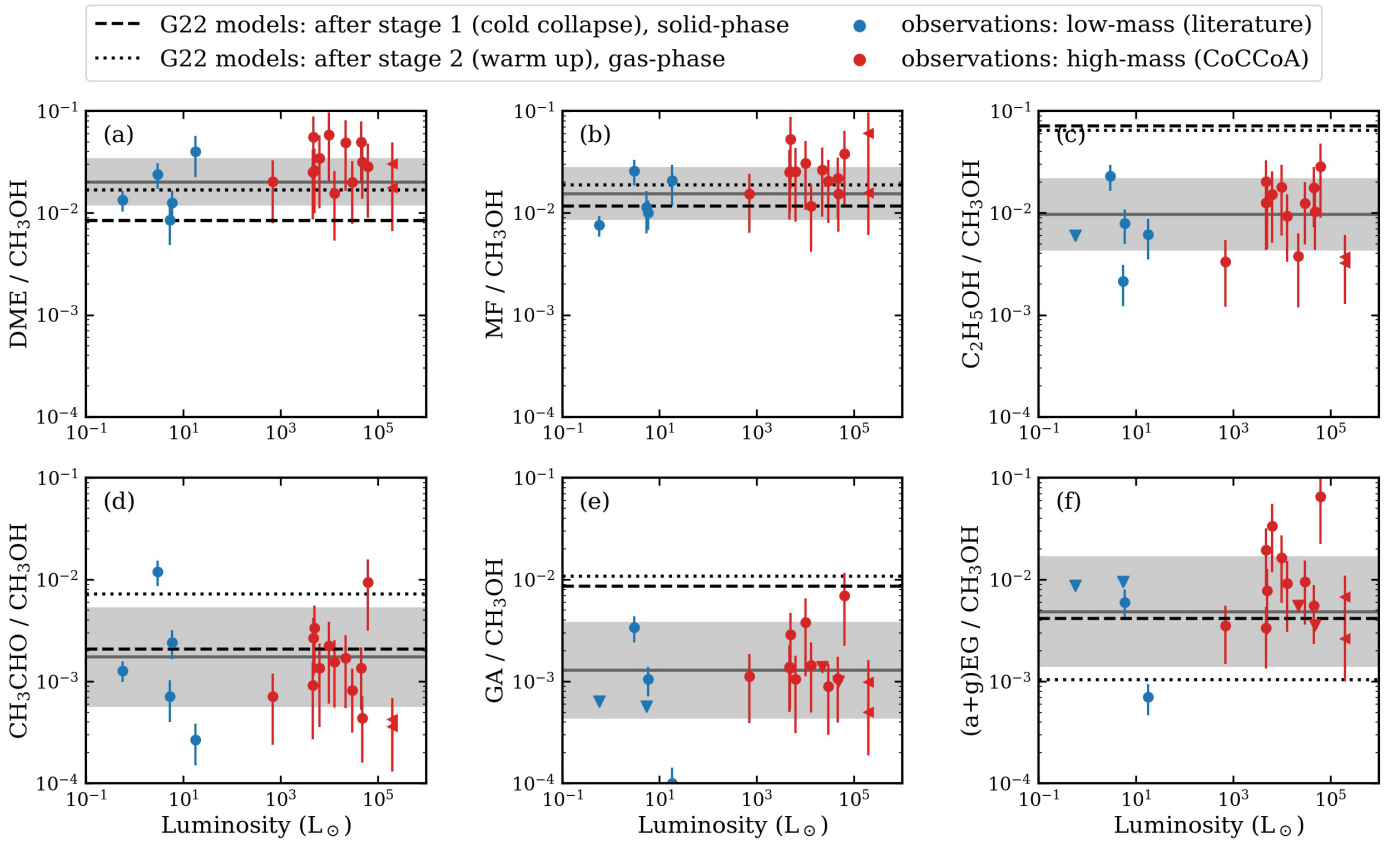

Fig. A.4: Same as Fig. 4 but includes the intercept error in Eq. (1).

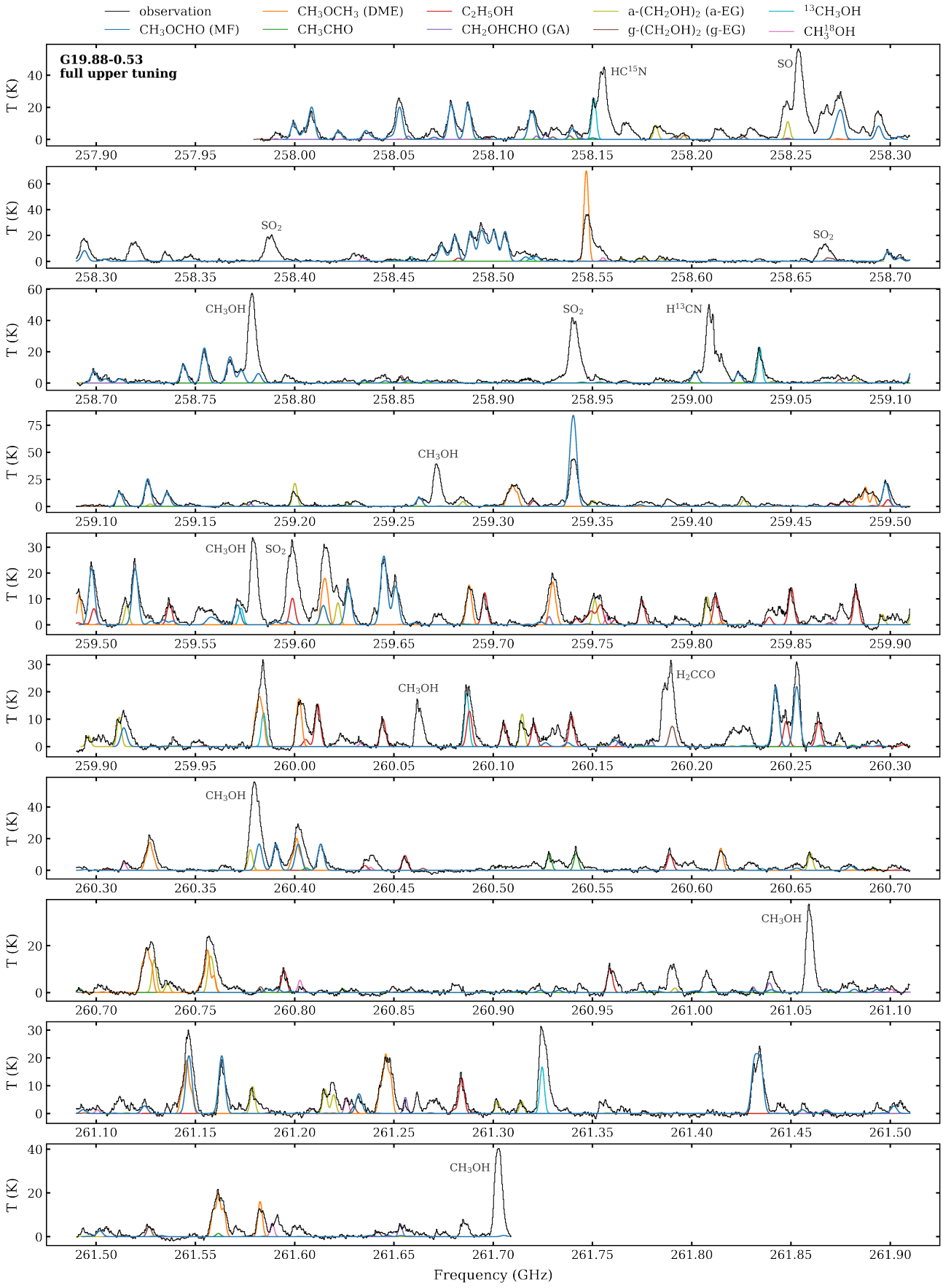

Fig. A.5: Same as Fig. 3 but for the full upper tuning. Some identified lines from species other than the selected O-COMs are labeled in gray text.

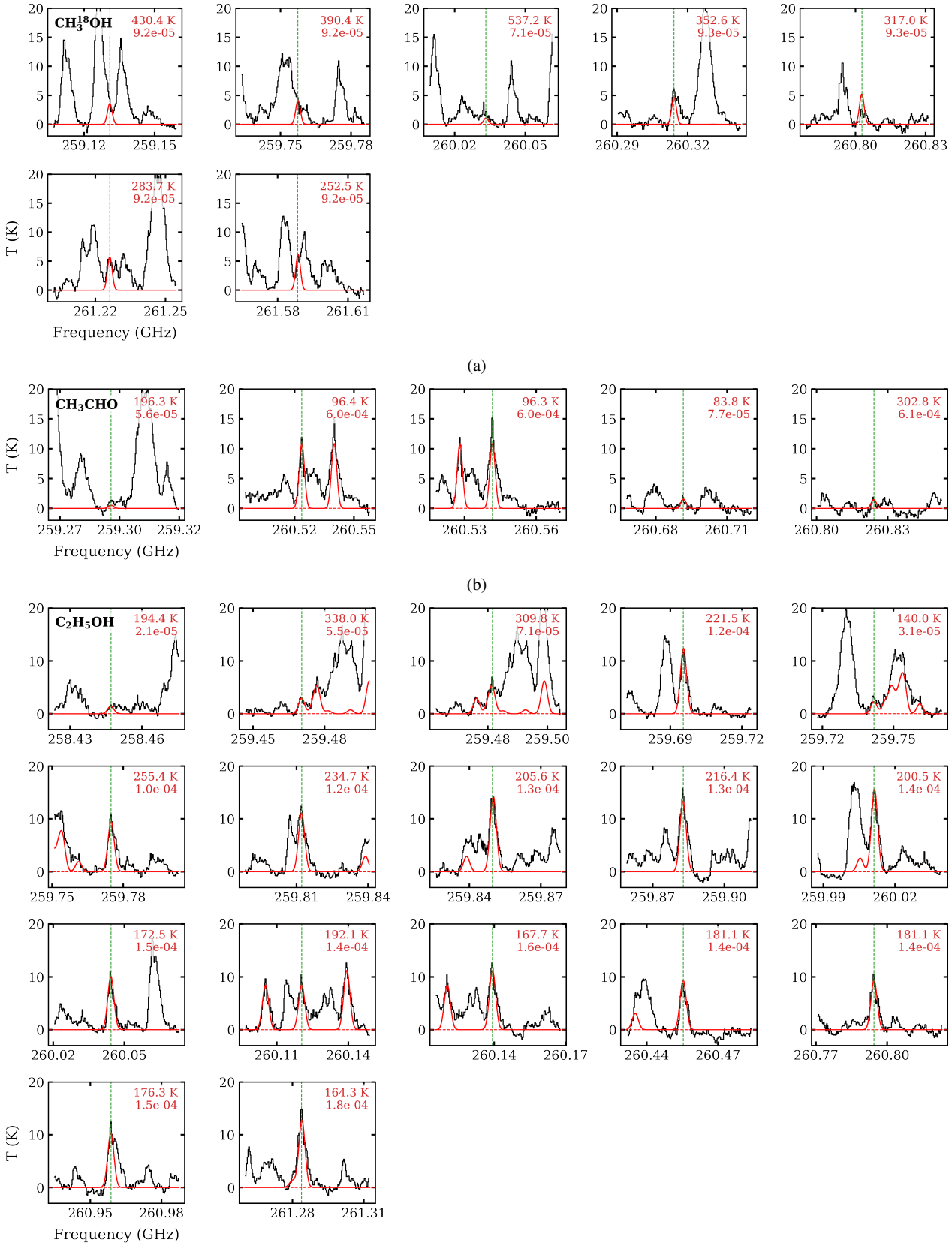

Fig. A.6: Best-fit model for $CH_3^{18}OH$, CH_3CHO, and C_2H_5OH, taking G19.88-0.53 as an example. Only selected unblended lines are shown. In each panel, the centered transition is indicated by the vertical dashed green line; the upper energy level (in K) and the Einstein A coefficient (in s^{-1}) are listed in red text in the upper right.

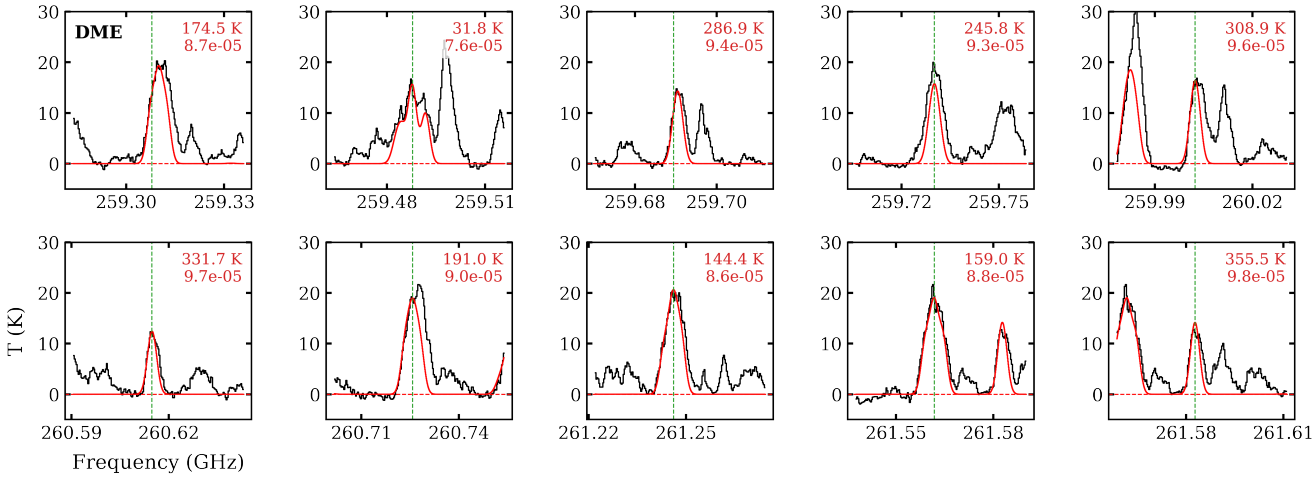

(a)

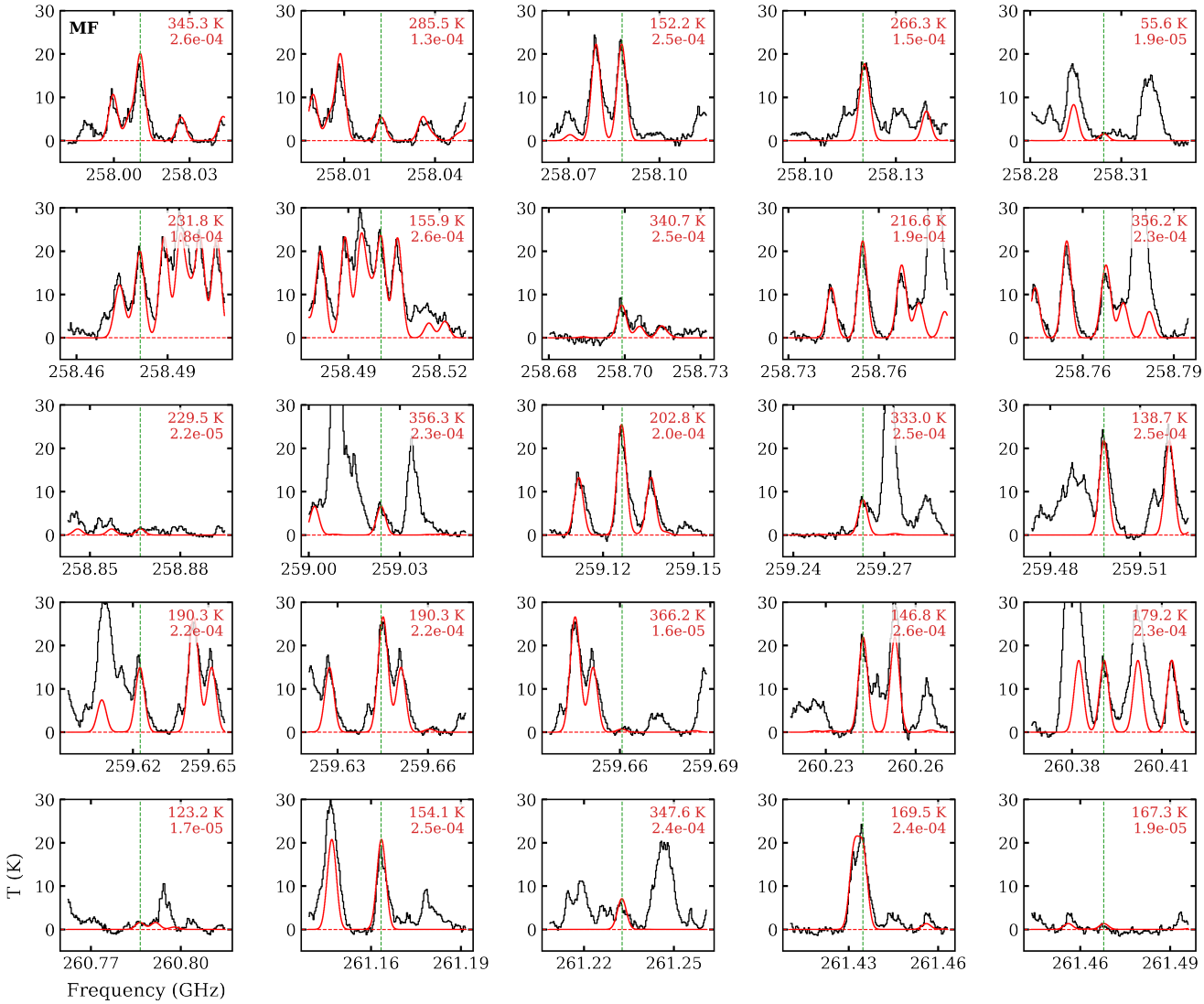

(b)

Fig. A.7: Same as Fig. A.6 but for CH_3OCH_3 (DME) and CH_3OCHO (MF).

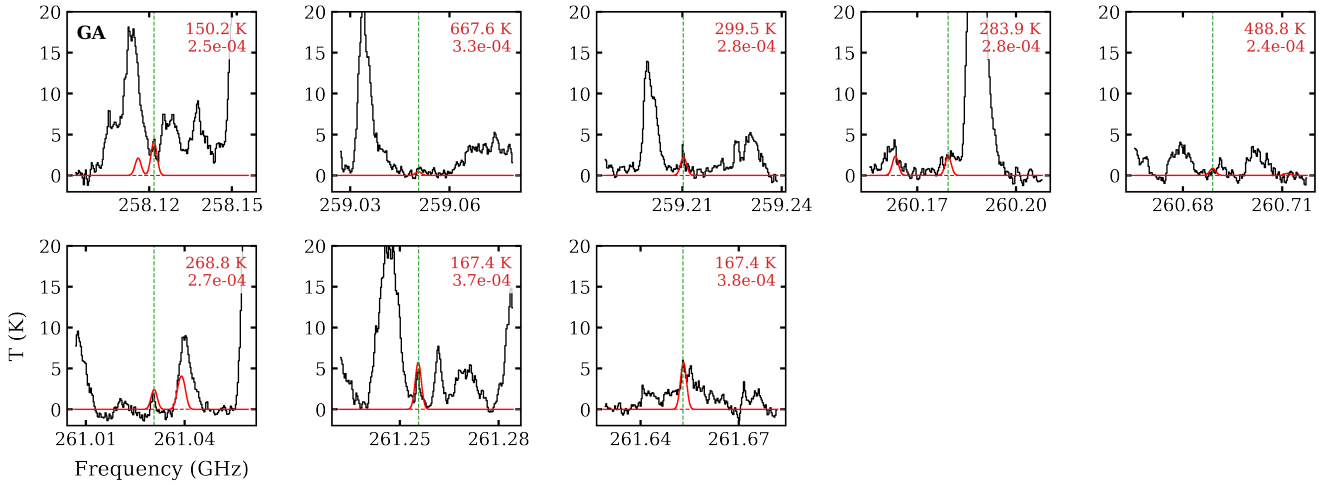

(a)

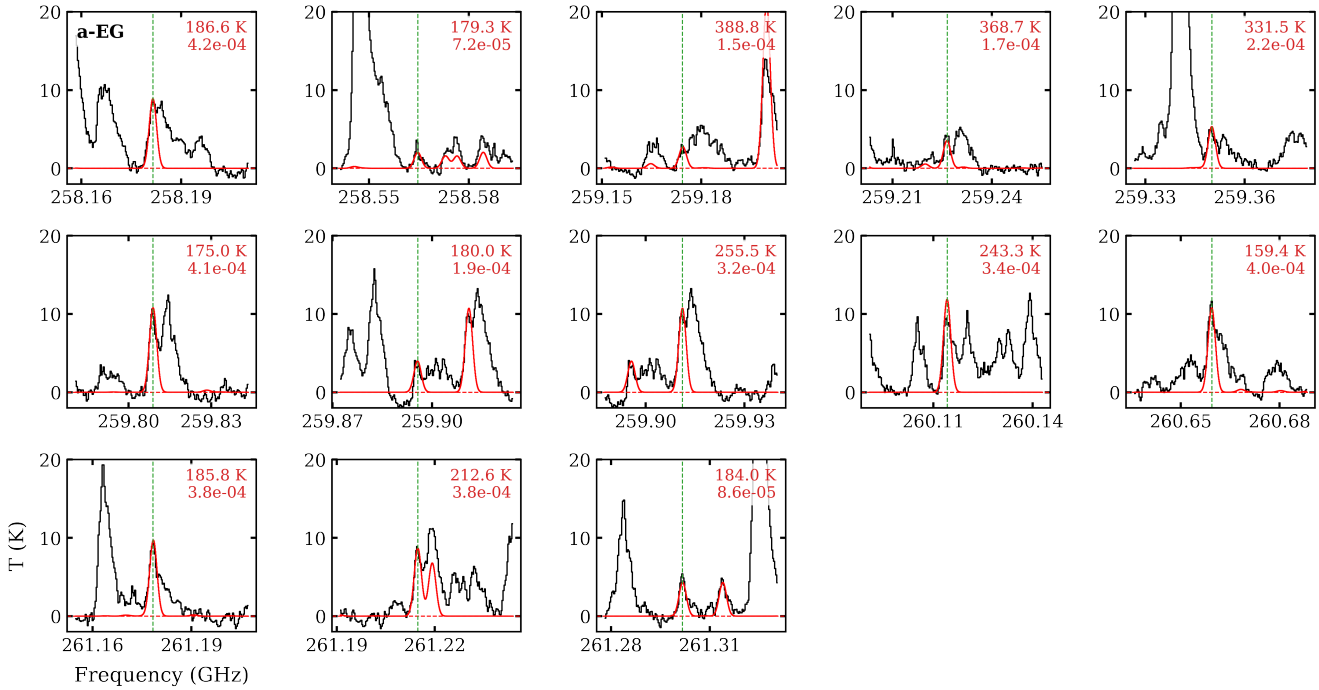

(b)

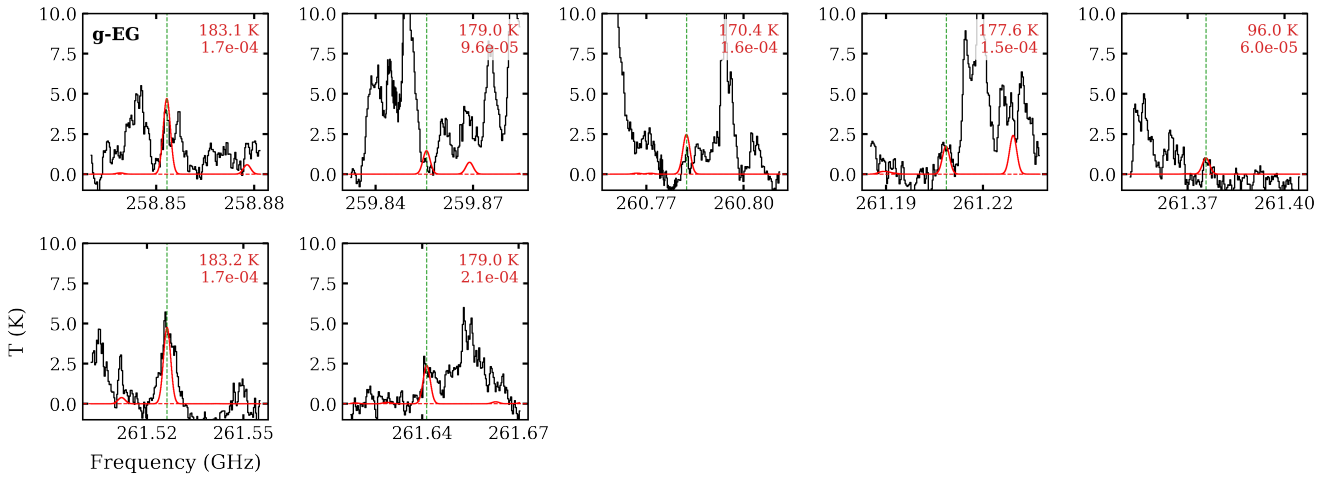

(c)

Fig. A.8: Same as Fig. A.6 but for CH_2OHCHO (GA) and *a*- and *g*-$(CH_2OH)_2$ (EG).

Appendix B: Additional tables

Tables B.1–B.4 give the fitting results of the selected O-COMs of the 14 CoCCoA sources. Table B.5 provides the column densities of GA and EG that were derived directly from the spectral fitting (i.e., without vibrational corrections). Table B.6 lists the identified transitions of two minor isotopologues of CH_3OH and the six selected O-COMs focused on in this paper.

Table B.1: Fitting results of $CH_3^{18}OH$ and CH_3CHO.

	CH_3OH^a	$CH_3^{18}OH$ (CDMS)^b				CH_3CHO (JPL)			
Source Name	N cm^{-2}	N (cm^{-2})	T_{ex} (K)	FWHM (km s^{-1})	v_{lsr} (km s^{-1})	N (cm^{-2})	T_{ex} (K)	FWHM (km s^{-1})	v_{lsr} (km s^{-1})
G19.01-0.03 (c1)^c	$(3.6\pm1.1)\times10^{18}$	$(1.2\pm0.3)\times10^{16}$	[180]^d	3.0	63.0				
G19.01-0.03 (c2)^c						$(8.0\pm3.0)\times10^{15}$	[150]	3.2	58.5
G19.88-0.53	$(4.4\pm1.3)\times10^{18}$	$(1.3\pm0.3)\times10^{16}$	[180]	2.7	46.2	$(4.0\pm1.5)\times10^{15}$	100±30	3.0	46.4
G22.04+0.22	$(1.3\pm0.4)\times10^{19}$	$(4.0\pm1.0)\times10^{16}$	[130]	4.5	53.5	$(4.5\pm1.0)\times10^{16}$	180±20	4.5	52.5
G23.21-0.37	$(2.6\pm0.7)\times10^{19}$	$(9.0\pm2.0)\times10^{16}$	[170]	3.0	76.8	$(4.0\pm0.6)\times10^{16}$	150±30	3.5	77.0
G34.30+0.20 (c1)	$(9.6\pm2.8)\times10^{18}$	$(2.2\pm0.5)\times10^{16}$	[140]	3.5	56.5	$(1.3\pm0.3)\times10^{16}$	130±20	3.5	56.3
G34.41+0.24 (c1)	$(7.9\pm2.3)\times10^{18}$	$(1.8\pm0.4)\times10^{16}$	[160]	3.5	60.0	$(1.2\pm0.3)\times10^{16}$	140±20	3.0	60.0
G34.41+0.24 (c2)						$(9.0\pm2.0)\times10^{15}$	[160]	3.0	56.8
G35.03+0.35	$(1.8\pm0.7)\times10^{18}$	$(4.5\pm1.5)\times10^{15}$	[150]	2.5	44.8	$(2.5\pm1.0)\times10^{15}$	110±30	4.0	44.8
G35.20-0.74N (c1)	$(8.2\pm2.5)\times10^{18}$	$(2.0\pm0.5)\times10^{16}$	[140]	3.5	31.0	$(5.0\pm1.0)\times10^{15}$	100±20	3.0	31.0
G35.20-0.74N (c2)						$(1.8\pm0.5)\times10^{15}$	100±20	1.7	33.5
G345.5+1.5	$(1.4\pm0.3)\times10^{18}$	$(3.2\pm0.5)\times10^{15}$	120±30	2.0	-15.8	$(6.0\pm2.0)\times10^{14}$	[120]	2.0	-16.3
IRAS 18151-1208	$(5.3\pm2.0)\times10^{17}$	$(1.5\pm0.5)\times10^{15}$	[180]	2.0	35.0	$(9.0\pm2.0)\times10^{14}$	150±30	2.0	35.0
IRAS 16547-4247	$(2.1\pm0.8)\times10^{18}$	$(6.0\pm2.0)\times10^{15}$	[200]	2.2	-35.5	$(2.0\pm0.4)\times10^{16}$	150±30	3.0	-35.5
NGC 6334-38	$(4.9\pm1.5)\times10^{18}$	$(1.2\pm0.3)\times10^{16}$	[120]	2.7	-5.0	$(1.8\pm0.5)\times10^{15}$	100±30	2.8	-5.1
NGC 6334-43	$(5.4\pm1.6)\times10^{18}$	$(1.3\pm0.3)\times10^{16}$	[160]	3.2	0.8	$(2.3\pm0.5)\times10^{15}$	100±50	3.0	1.0
NGC 6334 I(N)-SM2	$(3.9\pm1.1)\times10^{18}$	$(9.0\pm2.0)\times10^{15}$	[150]	3.0	-3.0	$(2.8\pm1.0)\times10^{15}$	80±30	3.0	-2.5

[a]The column density of the major isotopologue of methanol was inferred from the minor isotopologue $CH_3^{18}OH$ and the isotopic ratio between ^{16}O and ^{18}O.
[b]The spectroscopic databases used in the fitting.
[c]Component 1 and 2 (some sources exhibit two components in their spectra); see Fig. A.3 for an example.
[d]The T_{ex} in square brackets means that it was fixed to that value during the fitting. In this case, the uncertainties of N were determined only for this particular T_{ex}.

Table B.2: Fitting results of C_2H_5OH and CH_3OCH_3 (DME).

	C_2H_5OH (CDMS)				CH_3OCH_3 (CDMS)			
Source Name	N^a (cm^{-2})	T_{ex} (K)	FWHM (km s^{-1})	v_{lsr} (km s^{-1})	N^a (cm^{-2})	T_{ex} (K)	FWHM (km s^{-1})	v_{lsr} (km s^{-1})
G19.01-0.03 (c1)	(3.1±0.8)×10^{16}	160±40	3.2	62.3	(1.1±0.2)×10^{17}	130±20	3.8	61.8
G19.01-0.03 (c2)	(3.3±0.6)×10^{16}	160±40	3.2	58.5	(1.0±0.2)×10^{17}	130±20	3.5	57.8
G19.88-0.53	(5.5±1.5)×10^{16}	170±30	3.5	46.4	(1.1±0.3)×10^{17}	130±20	3.5	46.0
G22.04+0.22	(1.7±0.4)×10^{17}	[160]	5.5	53.0	(3.5±0.5)×10^{17}	120±20	5.5	52.3
G23.21-0.37	(2.4±0.4)×10^{17}	160±40	3.3	77.2	(4.0±0.8)×10^{17}	120±10	3.0	77.2
G34.30+0.20 (c1)	(1.2±0.3)×10^{17}	170±30	3.3	56.5	(3.7±0.6)×10^{17}	130±20	3.5	56.5
G34.30+0.20 (c2)	(5.0±1.0)×10^{16}	170±30	3.0	60.0	(1.1±0.3)×10^{17}	130±20	3.0	60.0
G34.41+0.24 (c1)	(8.0±2.0)×10^{16}	180±20	3.0	60.0	(2.2±0.3)×10^{17}	130±20	3.3	60.0
G34.41+0.24 (c2)	(8.0±2.0)×10^{16}	180±20	3.0	56.8	(2.2±0.3)×10^{17}	130±20	3.3	56.5
G35.03+0.35	(2.8±0.7)×10^{16}	120±40	3.5	44.6	(6.3±1.7)×10^{16}	130±20	3.7	45.0
G35.20-0.74N (c1)	(8.5±1.5)×10^{16}	160±20	4.0	31.2	(1.3±0.3)×10^{17}	130±20	4.0	31.0
G35.20-0.74N (c2)	(1.8±0.4)×10^{16}	160±20	1.5	33.7	(3.5±1.0)×10^{16}	130±20	1.7	33.7
G345.5+1.5	(1.4±0.3)×10^{16}	140±40	2.0	-16.3	(4.3±0.7)×10^{16}	120±20	2.0	-16.1
IRAS 18151-1208	(2.0±0.5)×10^{15}	[180]	1.9	35.3	(2.6±0.5)×10^{16}	110±20	2.0	35.1
IRAS 16547-4247	(6.0±1.5)×10^{16}	140±40	3.0	-35.2	(6.0±1.5)×10^{16}	180±20	2.7	-35.5
NGC 6334-38	(1.6±0.3)×10^{16}	190±50	2.6	-5.2	(1.5±0.3)×10^{17}	110±20	3.0	-5.2
NGC 6334-43	(2.0±0.5)×10^{16}	180±30	3.0	0.8	(9.5±2.5)×10^{16}	120±20	3.0	0.7
NGC 6334 I(N)-SM2	(1.3±0.4)×10^{16}	180±20	3.0	-3.0	(8.0±2.0)×10^{16}	100±20	4.5	-3.0

Table B.3: Fitting results of CH_3OCHO (MF) and CH_2OHCHO (GA).

	CH_3OCHO (JPL)				CH_2OHCHO (CDMS)			
Source Name	N (cm^{-2})	T_{ex} (K)	FWHM (km s^{-1})	v_{lsr} (km s^{-1})	N^a (cm^{-2})	T_{ex} (K)	FWHM (km s^{-1})	v_{lsr} (km s^{-1})
G19.01-0.03 (c1)	(5.0±1.0)×10^{16}	180±40	3.5	62.5	(7.0±2.3)×10^{15}	<120	3.5	61.5
G19.01-0.03 (c2)	(6.0±1.0)×10^{16}	180±40	3.5	58.5	(7.0±2.3)×10^{15}	<120	3.5	58.5
G19.88-0.53	(1.1±0.3)×10^{17}	180±40	4.0	46.0	(6.0±1.3)×10^{15}	160±40	2.5	46.4
G22.04+0.22	(7.0±2.0)×10^{17}	130±30	5.5	52.5	(3.9±0.8)×10^{16}	150±50	5.0	52.5
G23.21-0.37	(3.0±0.5)×10^{17}	170±30	3.3	77.2	(3.7±0.8)×10^{16}	200±40	3.5	76.8
G34.30+0.20 (c1)	(1.6±0.3)×10^{17}	140±40	3.2	56.5	(1.0±0.3)×10^{16}	180±30	3.5	55.5
G34.30+0.20 (c2)	(5.0±1.5)×10^{16}	140±40	2.5	60.0				
G34.41+0.24 (c1)	(1.0±0.2)×10^{17}	160±20	3.0	60.0				
G34.41+0.24 (c2)	(1.0±0.2)×10^{17}	160±20	3.0	56.8	(1.1±0.3)×10^{16}	160±40	3.0	57.0
G35.03+0.35	(4.7±1.3)×10^{16}	150±50	4.0	45.3	(2.0±0.7×10^{15}	[150]	3.5	44.5
G35.20-0.74N (c1)	(1.5±0.3)×10^{17}	140±30	4.0	31.2	(7.4±2.5)×10^{15}	[140]	3.5	31.2
G35.20-0.74N (c2)	(2.0±0.5)×10^{16}	140±30	1.2	33.7				
G345.5+1.5	(2.1±0.4)×10^{16}	120±20	2.2	-15.8	<1.4×10^{15}	[120]	2.2	-15.8
IRAS 18151-1208	(1.4±0.2)×10^{16}	180±40	2.0	35.2	<7.4×10^{14}	[180]	1.7	35.0
IRAS 16547-4247	(8.0±2.0)×10^{16}	200±20	3.3	-35.5	(1.5±0.3)×10^{16}	[200]	3.0	-35.5
NGC 6334-38	(3.0±0.5)×10^{17}	120±30	3.0	-5.2	(5.0±1.2)×10^{15}	140±70	2.8	-5.2
NGC 6334-43	(8.5±2.0)×10^{16}	160±40	3.0	0.8	(2.7±0.7)×10^{15}	[160]	3.0	0.8
NGC 6334 I(N)-SM2	(6.0±1.0)×10^{16}	150±30	5.0	-2.5	(4.4±1.5)×10^{15}	180±40	3.0	-2.5

[a]Vibrational corrections applied; see Table B.5 for the uncorrected N.

Table B.4: Fitting results of *a*-$(CH_2OH)_2$ (*a*-EG) and *g*-$(CH_2OH)_2$ (*g*-EG).

	a-$(CH_2OH)_2$ (CDMS)				g-$(CH_2OH)_2$ (CDMS)			
Source Name	N^a (cm^{-2})	T_{ex} (K)	FWHM (km s^{-1})	v_{lsr} (km s^{-1})	N^a (cm^{-2})	T_{ex} (K)	FWHM (km s^{-1})	v_{lsr} (km s^{-1})
G19.01-0.03 (c1)	$(4.0\pm0.8)\times10^{16}$	[180]	4.0	62.0	$(2.0\pm0.4)\times10^{16}$	[180]	3.5	61.0
G19.88-0.53	$(5.7\pm1.2)\times10^{16}$	220±20	3.0	46.7	$(2.9\pm0.7)\times10^{16}$	[220]	3.0	46.7
G22.04+0.22	$(5.9\pm1.5)\times10^{16}$	160±40	4.5	52.0	$(4.6\pm0.9)\times10^{16}$	[160]	4.5	52.0
G23.21-0.37	$(1.4\pm0.4)\times10^{17}$	180±40	3.8	77.0	$(1.0\pm0.4)\times10^{17}$	[180]	3.5	76.8
G34.30+0.20 (c1)	$(3.1\pm0.7)\times10^{16}$	[140]	3.5	55.5	$(2.2\pm0.5)\times10^{16}$	[140]	3.5	55.5
G34.41+0.24 (c1)	$(1.8\pm0.5)\times10^{16}$	160±40	3.0	60.8	$(8.2\pm1.8)\times10^{15}$	[160]	3.0	60.0
G35.03+0.35	$(4.3\pm1.0)\times10^{16}$	220±40	3.5	43.5	$(1.9\pm0.7)\times10^{16}$	[220]	3.5	43.5
G35.20-0.74N (c1)	$(5.3\pm1.6)\times10^{16}$	180±40	4.0	30.6	$(2.6\pm0.8)\times10^{16}$	[180]	3.5	30.6
G345.5+1.5	$<3.3\times10^{15}$	[120]	2.0	-15.0	$<1.6\times10^{15}$	[120]	2.0	-15.0
IRAS 18151-1208	$<1.0\times10^{15}$	[180]	2.0	35.0	$<2.0\times10^{15}$	[180]	2.0	35.0
IRAS 16547-4247	$(9.0\pm2.0)\times10^{16}$	180±40	3.2	-35.5	$(5.0\pm1.0)\times10^{16}$	[180]	3.0	-35.7
NGC 6334-38	$(6.5\pm1.6)\times10^{15}$	[120]	2.8	-5.2	$(6.5\pm2.4)\times10^{15}$	[120]	2.8	-5.2
NGC 6334-43	$(2.1\pm0.6)\times10^{16}$	200±40	3.0	0.8	$(1.5\pm0.4)\times10^{16}$	[200]	3.0	0.7
NGC 6334 I(N)-SM2	$(9.0\pm2.0)\times10^{15}$	180±50	4.0	-3.0	$<5.0\times10^{15}$	[180]	3.0	-3.0

[a]Vibrational corrections applied; see Table B.5 for the uncorrected *N*.

Table B.5: Column densities of CH_2OHCHO (GA) and *a*- and *g*-$(CH_2OH)_2$ (EG) without vibrational corrections.

Source Name	CH_2OHCHO N (cm^{-2})	a-$(CH_2OH)_2$ N (cm^{-2})	g-$(CH_2OH)_2$ N (cm^{-2})
G19.01-0.03 (c1, c2)	$(6.0\pm2.0)\times10^{15}$	$(2.0\pm0.4)\times10^{16}$	$(1.0\pm0.2)\times10^{16}$
G19.88-0.53	$(4.5\pm1.0)\times10^{15}$	$(2.4\pm0.5)\times10^{16}$	$(1.2\pm0.3)\times10^{16}$
G22.04+0.22	$(3.0\pm0.6)\times10^{16}$	$(3.2\pm0.8)\times10^{16}$	$(2.5\pm0.5)\times10^{16}$
G23.21-0.37	$(2.3\pm0.5)\times10^{16}$	$(7.0\pm2.0)\times10^{16}$	$(5.0\pm2.0)\times10^{16}$
G34.30+0.20	$(7.0\pm2.0)\times10^{15}$	$(1.8\pm0.4)\times10^{16}$	$(1.3\pm0.3)\times10^{16}$
G34.41+0.24	$(8.0\pm2.0)\times10^{15}$	$(1.0\pm0.3)\times10^{16}$	$(4.5\pm1.0)\times10^{15}$
G35.03+0.35	$(1.5\pm0.5)\times10^{15}$	$(1.8\pm0.4)\times10^{16}$	$(8.0\pm3.0)\times10^{15}$
G35.20-0.74N	$(6.0\pm2.0)\times10^{15}$	$(2.7\pm0.8)\times10^{16}$	$(1.3\pm0.4)\times10^{16}$
G345.5+1.5	$<1.2\times10^{15}$	$<2.0\times10^{15}$	$<1.0\times10^{15}$
IRAS 18151-1208	$<5.0\times10^{14}$	$<5.0\times10^{14}$	$<1.0\times10^{15}$
IRAS 16547-4247	$(9.0\pm2.0)\times10^{15}$	$(4.5\pm1.0)\times10^{16}$	$(2.5\pm0.5)\times10^{16}$
NGC 6334-38	$(4.0\pm1.0)\times10^{15}$	$(4.0\pm1.0)\times10^{15}$	$(4.0\pm1.5)\times10^{15}$
NGC 6334-43	$(2.0\pm0.5)\times10^{15}$	$(1.0\pm0.3)\times10^{16}$	$(7.0\pm2.0)\times10^{15}$
NGC 6334 I(N)-SM2	$(3.0\pm1.0)\times10^{15}$	$(4.5\pm1.0)\times10^{15}$	$<2.5\times10^{15}$

Table B.6: Identified transitions of O-COMs.

Species Database	Transition			Frequency (MHz)	E_{up} (K)	A_{ij} (s^{-1}) $a(b) = a \times 10^b$
$^{13}CH_3OH$, vt=0,1	16 3 14 +0	–	16 2 15 -0	258153.004	358.01	9.03(-5)
CDMS	19 5 15 +0	–	20 4 16 +0	258460.830	568.65	2.95(-5)
	19 5 14 -0	–	20 4 17 -0	258521.376	568.65	2.95(-5)
	17 3 15 +0	–	17 2 16 -0	259036.489	396.48	9.11(-5)
	12 -2 10 1	–	13 -3 10 1	259575.198	540.96	7.21(-5)
	2 1 1 0	–	1 0 1 0	259986.530	27.85	5.46(-5)
	18 3 16 +0	–	18 2 17 -0	260088.839	437.21	9.21(-5)
	24 -3 21 1	–	23 -2 21 1	260637.531	999.80	6.76(-5)
	19 3 17 +0	–	19 2 18 -0	261326.838	480.20	9.31(-5)
$CH_3^{18}OH$, v=0-2	19 3 16 0	–	19 2 17 0	258436.476	472.65	9.22(-5)
CDMS	15 1 14 0	–	14 2 13 0	258557.479	283.36	4.05(-5)
	18 3 15 0	–	18 2 16 0	259133.097	430.41	9.24(-5)
	5 4 2 1	–	6 3 4 1	259391.755	121.80	8.35(-6)
	17 3 14 0	–	17 2 15 0	259759.660	390.39	9.25(-5)
	17 2 15 2	–	16 3 13 2	259873.428	362.98	2.95(-5)
	12 2 10 4	–	13 3 10 4	260035.462	537.16	7.08(-5)
	16 3 13 0	–	16 2 14 0	260316.321	352.59	9.26(-5)
	15 1 15 1	–	14 2 13 1	260440.344	272.16	2.76(-5)
	15 3 12 0	–	15 2 13 0	260804.867	317.02	9.26(-5)
	15 4 11 2	–	16 3 13 2	261102.783	363.04	3.00(-5)
	14 3 11 0	–	14 2 12 0	261228.369	283.66	9.25(-5)
	13 3 10 0	–	13 2 11 0	261590.879	252.53	9.24(-5)
CH_3CHO	19 3 17 1	–	19 2 18 1	259298.775	196.31	5.60(-5)
JPL	13 1 12 6	–	12 1 11 6	259375.784	459.31	5.70(-4)
	13 2 12 7	–	12 2 11 7	259761.410	474.77	5.34(-4)
	19 3 17 0	–	19 2 18 0	260283.405	196.35	5.69(-5)
	13 1 13 1	–	12 0 12 2	260408.016	83.89	7.68(-5)
	14 1 14 1	–	13 1 13 1	260530.403	96.39	6.02(-4)
	14 1 14 0	–	13 1 13 0	260544.019	96.32	6.01(-4)
	13 1 13 0	–	12 0 12 0	260694.002	83.82	7.73(-5)
	14 1 14 3	–	13 1 13 3	260826.516	302.82	6.12(-4)
C_2H_5OH, v=0	19 2 18 1	–	18 3 16 0	258099.207	222.51	1.42(-5)
CDMS	16 4 13 1	–	16 3 13 0	258449.274	194.44	2.12(-5)
	25 1 24 2	–	25 0 25 2	258484.664	272.70	3.90(-5)
	14 3 11 0	–	13 2 11 1	259322.639	155.72	7.25(-5)
	15 12 3 1	–	14 12 2 1	259472.683	337.99	5.52(-5)
	15 12 4 1	–	14 12 3 1	259472.683	337.99	5.52(-5)
	15 13 2 1	–	14 13 1 1	259477.660	368.56	3.81(-5)
	15 13 3 1	–	14 13 2 1	259477.660	368.56	3.81(-5)
	15 11 4 1	–	14 11 3 1	259479.315	309.83	7.09(-5)
	15 11 5 1	–	14 11 4 1	259479.315	309.83	7.09(-5)
	15 10 5 1	–	14 10 4 1	259501.052	284.11	8.53(-5)
	15 10 6 1	–	14 10 5 1	259501.052	284.11	8.53(-5)
	15 9 6 1	–	14 9 5 1	259539.131	260.82	9.82(-5)
	15 9 7 1	–	14 9 6 1	259539.131	260.82	9.82(-5)
	15 8 8 1	–	14 8 7 1	259601.059	239.96	1.10(-4)
	15 8 7 1	–	14 8 6 1	259601.060	239.96	1.10(-4)
	15 7 9 1	–	14 7 8 1	259697.897	221.55	1.20(-4)
	15 7 8 1	–	14 7 7 1	259697.903	221.55	1.20(-4)
	13 1 12 1	–	12 2 10 0	259744.133	140.01	3.11(-5)
	18 4 15 1	–	18 3 15 0	259748.793	223.63	3.48(-5)
	15 11 4 0	–	14 11 3 0	259751.561	304.31	7.53(-5)
	15 11 5 0	–	14 11 4 0	259751.561	304.31	7.53(-5)
	15 12 3 0	–	14 12 2 0	259754.443	332.42	5.88(-5)
	15 12 4 0	–	14 12 3 0	259754.443	332.42	5.88(-5)
	15 10 5 0	–	14 10 4 0	259756.535	278.65	9.03(-5)
	15 10 6 0	–	14 10 5 0	259756.535	278.65	9.03(-5)
	15 13 2 0	–	14 13 1 0	259763.493	362.98	4.08(-5)
	15 13 3 0	–	14 13 2 0	259763.493	362.98	4.08(-5)

Table B.6: continued.

Species Database	Transition			Frequency (MHz)	E_{up} (K)	A_{ij} (s^{-1}) $a(b) = a \times 10^b$
	15 9 6 0	–	14 9 5 0	259777.143	255.43	1.04(-4)
	15 9 7 0	–	14 9 6 0	259777.143	255.43	1.04(-4)
	15 14 1 0	–	14 14 0 0	259778.002	395.98	2.13(-5)
	15 14 2 0	–	14 14 1 0	259778.002	395.98	2.13(-5)
	15 8 8 0	–	14 8 7 0	259814.437	234.67	1.16(-4)
	15 8 7 0	–	14 8 6 0	259814.438	234.67	1.16(-4)
	32 5 28 2	–	32 4 29 2	259841.221	477.18	1.17(-4)
	15 6 10 1	–	14 6 9 1	259852.185	205.59	1.29(-4)
	15 6 9 1	–	14 6 8 1	259852.573	205.59	1.29(-4)
	15 7 9 0	–	14 7 8 0	259885.072	216.37	1.27(-4)
	15 7 8 0	–	14 7 7 0	259885.079	216.37	1.27(-4)
	25 2 24 2	–	25 1 25 2	260007.736	272.77	3.96(-5)
	15 6 10 0	–	14 6 9 0	260013.579	200.53	1.36(-4)
	15 6 9 0	–	14 6 8 0	260014.001	200.53	1.36(-4)
	15 3 13 1	–	14 3 12 1	260046.644	172.46	1.46(-4)
	15 1 14 0	–	14 1 13 0	260090.201	159.58	1.75(-4)
	15 5 11 1	–	14 5 10 1	260107.609	192.10	1.37(-4)
	15 5 10 1	–	14 5 9 1	260122.761	192.10	1.37(-4)
	15 3 13 0	–	14 3 12 0	260141.678	167.72	1.59(-4)
	15 5 11 0	–	14 5 10 0	260249.761	187.15	1.45(-4)
	15 5 10 0	–	14 5 9 0	260266.127	187.15	1.45(-4)
	7 1 6 1	–	6 0 6 0	260437.554	86.70	5.46(-5)
	15 4 12 1	–	14 4 11 1	260457.726	181.10	1.43(-4)
	15 4 12 0	–	14 4 11 0	260591.330	176.26	1.52(-4)
	31 4 28 2	–	30 5 25 2	260627.301	437.93	1.86(-5)
	15 4 11 1	–	14 4 10 1	260796.868	181.14	1.43(-4)
	15 4 11 0	–	14 4 10 0	260960.989	176.30	1.53(-4)
	20 3 18 1	–	19 4 16 0	261282.323	247.21	2.17(-5)
	15 1 14 1	–	14 1 13 1	261286.306	164.30	1.79(-4)
CH_3OCH_3 (DME), v=0 CDMS	30 5 26 3	–	29 6 23 3	258197.879	459.88	2.47(-5)
	30 5 26 5	–	29 6 23 5	258197.880	459.88	2.47(-5)
	30 5 26 1	–	29 6 23 1	258198.172	459.88	2.47(-5)
	30 5 26 0	–	29 6 23 0	258198.464	459.88	2.47(-5)
	30 14 17 3	–	31 15 17 3	258278.183	738.73	1.24(-5)
	14 1 14 3	–	13 0 13 3	258548.819	93.33	1.31(-4)
	14 1 14 5	–	13 0 13 5	258548.819	93.33	1.31(-4)
	14 1 14 1	–	13 0 13 1	258549.063	93.33	1.31(-4)
	14 1 14 0	–	13 0 13 0	258549.308	93.33	1.31(-4)
	17 5 12 5	–	17 4 13 5	259309.472	174.54	8.77(-5)
	17 5 12 3	–	17 4 13 3	259309.758	174.54	8.74(-5)
	17 5 12 1	–	17 4 13 1	259311.947	174.54	8.76(-5)
	17 5 12 0	–	17 4 13 0	259314.279	174.54	8.77(-5)
	6 3 4 3	–	5 2 3 3	259484.856	31.77	7.40(-5)
	6 3 4 5	–	5 2 3 5	259486.616	31.77	7.65(-5)
	6 3 4 1	–	5 2 3 1	259489.733	31.77	7.58(-5)
	6 3 4 0	–	5 2 3 0	259493.749	31.77	7.65(-5)
	22 5 18 3	–	22 4 19 3	259615.889	265.87	9.34(-5)
	22 5 18 5	–	22 4 19 5	259615.896	265.87	9.34(-5)
	22 5 18 1	–	22 4 19 1	259617.339	265.87	9.34(-5)
	22 5 18 0	–	22 4 19 0	259618.785	265.87	9.34(-5)
	23 5 19 3	–	23 4 20 3	259688.831	286.90	9.44(-5)
	23 5 19 5	–	23 4 20 5	259688.835	286.90	9.44(-5)
	23 5 19 1	–	23 4 20 1	259690.065	286.90	9.44(-5)
	23 5 19 0	–	23 4 20 0	259691.297	286.90	9.44(-5)
	21 5 17 3	–	21 4 18 3	259730.487	245.76	9.26(-5)
	21 5 17 5	–	21 4 18 5	259730.502	245.76	9.26(-5)
	21 5 17 1	–	21 4 18 1	259732.149	245.76	9.26(-5)
	21 5 17 0	–	21 4 18 0	259733.804	245.76	9.26(-5)
	33 6 28 3	–	32 7 25 3	259816.557	562.74	2.54(-5)

Table B.6: continued.

Species Database	Transition			Frequency (MHz)	E_{up} (K)	A_{ij} (s^{-1}) $a(b) = a \times 10^b$
	33 6 28 5	–	32 7 25 5	259816.583	562.74	2.54(-5)
	33 6 28 1	–	32 7 25 1	259817.273	562.74	2.54(-5)
	33 6 28 0	–	32 7 25 0	259817.976	562.74	2.54(-5)
	20 5 16 3	–	20 4 17 3	259982.535	226.58	9.18(-5)
	20 5 16 5	–	20 4 17 5	259982.568	226.58	9.18(-5)
	20 5 16 1	–	20 4 17 1	259984.408	226.58	9.18(-5)
	20 5 16 0	–	20 4 17 0	259986.265	226.58	9.18(-5)
	24 5 20 3	–	24 4 21 3	260003.375	308.85	9.55(-5)
	24 5 20 5	–	24 4 21 5	260003.377	308.85	9.55(-5)
	24 5 20 1	–	24 4 21 1	260004.389	308.85	9.55(-5)
	24 5 20 0	–	24 4 21 0	260005.402	308.85	9.55(-5)
	19 5 15 3	–	19 4 16 3	260327.133	208.31	9.10(-5)
	19 5 15 5	–	19 4 16 5	260327.201	208.31	9.10(-5)
	19 5 15 1	–	19 4 16 1	260329.221	208.31	9.10(-5)
	19 5 15 0	–	19 4 16 0	260331.275	208.31	9.10(-5)
	16 5 11 5	–	16 4 12 5	260400.539	159.03	8.73(-5)
	16 5 11 3	–	16 4 12 3	260401.135	159.03	8.64(-5)
	16 5 11 1	–	16 4 12 1	260403.244	159.03	8.71(-5)
	16 5 11 0	–	16 4 12 0	260405.649	159.03	8.73(-5)
	25 5 21 3	–	25 4 22 3	260616.059	331.72	9.68(-5)
	25 5 21 5	–	25 4 22 5	260616.059	331.72	9.68(-5)
	25 5 21 1	–	25 4 22 1	260616.851	331.72	9.68(-5)
	25 5 21 0	–	25 4 22 0	260617.643	331.72	9.68(-5)
	18 5 14 3	–	18 4 15 3	260725.448	190.97	9.02(-5)
	18 5 14 5	–	18 4 15 5	260725.587	190.97	9.02(-5)
	18 5 14 1	–	18 4 15 1	260727.767	190.97	9.02(-5)
	18 5 14 0	–	18 4 15 0	260730.017	190.97	9.02(-5)
	6 3 3 5	–	5 2 4 5	260754.380	31.77	7.71(-5)
	6 3 3 3	–	5 2 4 3	260756.140	31.77	7.47(-5)
	6 3 3 1	–	5 2 4 1	260758.402	31.77	7.65(-5)
	6 3 3 0	–	5 2 4 0	260761.524	31.77	7.72(-5)
	17 5 13 3	–	17 4 14 3	261145.206	174.54	8.91(-5)
	17 5 13 5	–	17 4 14 5	261145.492	174.54	8.94(-5)
	17 5 13 1	–	17 4 14 1	261147.803	174.54	8.93(-5)
	17 5 13 0	–	17 4 14 0	261150.257	174.54	8.94(-5)
	15 5 10 5	–	15 4 11 5	261245.097	144.44	8.66(-5)
	15 5 10 3	–	15 4 11 3	261246.331	144.44	8.30(-5)
	15 5 10 1	–	15 4 11 1	261248.113	144.44	8.56(-5)
	15 5 10 0	–	15 4 11 0	261250.488	144.44	8.66(-5)
	16 5 12 3	–	16 4 13 3	261560.797	159.03	8.74(-5)
	16 5 12 5	–	16 4 13 5	261561.393	159.03	8.84(-5)
	16 5 12 1	–	16 4 13 1	261563.781	159.03	8.81(-5)
	16 5 12 0	–	16 4 13 0	261566.471	159.03	8.84(-5)
	26 5 22 3	–	26 4 23 3	261584.210	355.51	9.84(-5)
	26 5 22 5	–	26 4 23 5	261584.210	355.51	9.84(-5)
	26 5 22 1	–	26 4 23 1	261584.781	355.51	9.84(-5)
	26 5 22 0	–	26 4 23 0	261585.353	355.51	9.84(-5)
CH_3OCHO (MF)	21 8 13 3	–	20 8 12 3	257906.128	365.98	2.22(-4)
JPL	21 16 5 0	–	20 16 4 0	257910.566	306.01	1.09(-4)
	21 16 6 0	–	20 16 5 0	257910.566	306.01	1.09(-4)
	21 16 5 2	–	20 16 4 2	257919.890	306.01	1.09(-4)
	21 16 6 1	–	20 16 5 1	257933.830	306.00	1.09(-4)
	21 15 6 0	–	20 15 5 0	258001.757	285.47	1.28(-4)
	21 15 7 0	–	20 15 6 0	258001.757	285.47	1.28(-4)
	21 15 6 2	–	20 15 5 2	258007.150	285.47	1.28(-4)
	24 0 24 3	–	23 1 23 3	258010.378	345.26	4.19(-5)
	24 1 24 3	–	23 1 23 3	258010.754	345.26	2.59(-4)
	24 0 24 3	–	23 0 23 3	258010.754	345.26	2.59(-4)
	24 1 24 3	–	23 0 23 3	258011.019	345.26	4.19(-5)

Table B.6: continued.

Species Database	Transition			Frequency (MHz)	E_{up} (K)	A_{ij} (s^{-1}) $a(b) = a \times 10^b$
	21 15 7 1	–	20 15 6 1	258024.240	285.46	1.28(-4)
	21 9 13 4	–	20 9 12 4	258037.974	376.94	2.13(-4)
	24 10 15 1	–	24 9 16 1	258041.077	243.70	2.22(-5)
	24 10 14 2	–	24 9 15 2	258049.562	243.71	2.22(-5)
	24 10 14 0	–	24 9 15 0	258052.000	243.70	2.23(-5)
	24 0 24 5	–	23 1 23 4	258054.742	344.52	4.10(-5)
	24 1 24 4	–	23 1 23 4	258055.043	344.52	2.60(-4)
	24 0 24 5	–	23 0 23 5	258055.043	344.52	2.60(-4)
	24 1 24 4	–	23 0 23 5	258055.296	344.52	4.10(-5)
	24 10 15 0	–	24 9 16 0	258072.452	243.70	2.23(-5)
	22 2 20 2	–	21 2 19 2	258081.042	152.23	2.52(-4)
	22 2 20 0	–	21 2 19 0	258089.491	152.22	2.52(-4)
	21 14 7 0	–	20 14 6 0	258121.191	266.26	1.45(-4)
	21 14 8 0	–	20 14 7 0	258121.191	266.26	1.45(-4)
	21 14 7 2	–	20 14 6 2	258122.660	266.25	1.45(-4)
	21 14 8 1	–	20 14 7 1	258142.090	266.25	1.45(-4)
	21 13 8 2	–	20 13 7 2	258274.950	248.38	1.61(-4)
	21 13 8 0	–	20 13 7 0	258277.434	248.38	1.61(-4)
	21 13 9 0	–	20 13 8 0	258277.434	248.38	1.61(-4)
	21 13 9 1	–	20 13 8 1	258296.300	248.36	1.61(-4)
	11 5 7 0	–	10 4 6 0	258306.279	55.60	1.92(-5)
	27 10 17 3	–	27 9 18 3	258380.810	476.33	2.37(-5)
	27 10 18 4	–	27 9 19 4	258425.612	476.33	2.36(-5)
	18 4 15 4	–	17 3 14 5	258450.614	298.62	1.49(-5)
	23 1 22 2	–	22 2 21 1	258475.052	155.91	3.57(-5)
	21 12 9 2	–	20 12 8 2	258476.450	231.83	1.76(-4)
	23 1 22 0	–	22 2 21 0	258480.586	155.90	3.57(-5)
	21 12 9 0	–	20 12 8 0	258482.981	231.83	1.76(-4)
	21 12 10 0	–	20 12 9 0	258482.981	231.83	1.76(-4)
	23 2 22 1	–	22 2 21 1	258490.870	155.91	2.57(-4)
	27 10 18 3	–	27 9 19 3	258493.927	476.33	2.38(-5)
	23 2 22 0	–	22 2 21 0	258496.242	155.90	2.57(-4)
	21 12 10 1	–	20 12 9 1	258499.332	231.82	1.76(-4)
	23 1 22 2	–	22 1 21 2	258502.735	155.91	2.57(-4)
	23 1 22 0	–	22 1 21 0	258508.181	155.90	2.57(-4)
	23 2 22 1	–	22 1 21 2	258518.554	155.91	3.57(-5)
	23 2 22 0	–	22 1 21 0	258523.821	155.90	3.57(-5)
	41 8 34 0	–	41 7 35 0	258541.136	557.04	2.34(-5)
	21 5 17 3	–	20 5 16 3	258701.047	340.65	2.46(-4)
	22 3 20 1	–	21 2 19 2	258706.904	152.26	2.85(-5)
	22 3 20 0	–	21 2 19 0	258714.075	152.25	2.85(-5)
	21 11 10 2	–	20 11 9 2	258746.248	216.63	1.91(-4)
	21 11 11 0	–	20 11 10 0	258756.673	216.63	1.91(-4)
	21 11 10 0	–	20 11 9 0	258756.673	216.63	1.91(-4)
	21 7 15 3	–	20 7 14 3	258768.938	356.20	2.33(-4)
	21 11 11 1	–	20 11 10 1	258769.974	216.62	1.91(-4)
	21 3 18 3	–	20 3 17 3	258775.320	333.28	2.52(-4)
	21 8 14 4	–	20 8 13 4	258783.896	365.70	2.25(-4)
	23 10 14 1	–	23 9 15 1	258837.620	229.45	2.20(-5)
	23 10 13 2	–	23 9 14 2	258847.920	229.46	2.20(-5)
	23 10 13 0	–	23 9 14 0	258859.163	229.46	2.20(-5)
	23 10 14 0	–	23 9 15 0	258868.739	229.46	2.20(-5)
	11 5 7 4	–	10 4 7 4	258955.739	242.40	1.97(-5)
	21 7 14 3	–	20 7 13 3	259003.875	356.22	2.34(-4)
	21 7 14 5	–	20 7 13 5	259025.827	356.29	2.34(-4)
	21 10 11 2	–	20 10 10 2	259113.950	202.78	2.04(-4)
	21 10 12 0	–	20 10 11 0	259128.178	202.78	2.04(-4)
	21 10 11 0	–	20 10 10 0	259128.178	202.78	2.04(-4)
	21 10 12 1	–	20 10 11 1	259137.930	202.77	2.04(-4)

Table B.6: continued.

Species Database	Transition			Frequency (MHz)	E_{up} (K)	A_{ij} (s^{-1}) $a(b) = a \times 10^b$
	21 3 18 5	–	20 3 17 5	259264.990	333.04	2.54(-4)
	34 4 30 0	–	34 3 31 0	259299.779	366.21	1.61(-5)
	24 0 24 2	–	23 1 23 1	259341.865	158.23	4.24(-5)
	24 1 24 1	–	23 1 23 1	259342.015	158.23	2.63(-4)
	24 0 24 2	–	23 0 23 2	259342.143	158.23	2.63(-4)
	24 1 24 1	–	23 0 23 2	259342.293	158.23	4.24(-5)
	24 0 24 0	–	23 1 23 0	259342.727	158.22	4.24(-5)
	24 1 24 0	–	23 1 23 0	259342.876	158.22	2.63(-4)
	24 0 24 0	–	23 0 23 0	259343.004	158.22	2.63(-4)
	24 1 24 0	–	23 0 23 0	259343.152	158.22	4.24(-5)
	11 5 6 0	–	10 4 7 0	259376.253	55.61	1.94(-5)
	42 7 35 2	–	42 6 36 2	259422.473	581.45	2.31(-5)
	11 5 6 2	–	10 4 7 1	259445.549	55.62	1.08(-5)
	26 10 17 3	–	26 9 18 3	259455.455	460.41	2.36(-5)
	42 7 35 0	–	42 6 36 0	259463.004	581.46	2.31(-5)
	20 4 16 2	–	19 4 15 2	259499.905	138.67	2.54(-4)
	20 4 16 0	–	19 4 15 0	259521.812	138.67	2.54(-4)
	22 10 13 1	–	22 9 14 1	259529.940	215.81	2.16(-5)
	22 3 19 2	–	21 4 18 1	259536.089	159.72	2.05(-5)
	22 10 12 2	–	22 9 13 2	259540.700	215.82	2.16(-5)
	22 10 12 0	–	22 9 13 0	259558.582	215.81	2.16(-5)
	22 3 19 0	–	21 4 18 0	259560.402	159.72	2.05(-5)
	22 10 13 0	–	22 9 14 0	259562.851	215.81	2.16(-5)
	21 5 17 4	–	20 5 16 4	259573.430	340.45	2.49(-4)
	34 5 30 1	–	34 4 31 1	259592.949	366.22	1.62(-5)
	26 10 17 4	–	26 9 18 4	259593.370	460.37	2.35(-5)
	21 6 16 3	–	20 6 15 3	259616.603	347.84	2.43(-4)
	21 9 12 2	–	20 9 11 2	259629.300	190.30	2.16(-4)
	21 9 13 0	–	20 9 12 0	259646.531	190.29	2.17(-4)
	21 9 12 0	–	20 9 11 0	259647.705	190.29	2.17(-4)
	21 9 13 1	–	20 9 12 1	259653.078	190.28	2.17(-4)
	34 5 30 0	–	34 4 31 0	259662.604	366.23	1.62(-5)
	21 7 15 4	–	20 7 14 4	259916.051	355.90	2.37(-4)
	21 10 12 1	–	21 9 13 1	260128.610	202.77	2.12(-5)
	21 10 11 2	–	21 9 12 2	260139.772	202.78	2.12(-5)
	21 10 11 0	–	21 9 12 0	260162.612	202.78	2.12(-5)
	21 10 12 0	–	21 9 13 0	260164.454	202.78	2.12(-5)
	21 3 18 2	–	20 3 17 2	260244.498	146.76	2.56(-4)
	21 3 18 0	–	20 3 17 0	260255.080	146.75	2.56(-4)
	25 10 16 3	–	25 9 17 3	260296.709	445.09	2.34(-5)
	21 8 13 2	–	20 8 12 2	260384.268	179.20	2.28(-4)
	21 8 14 0	–	20 8 13 0	260392.731	179.19	2.29(-4)
	21 8 14 1	–	20 8 13 1	260404.026	179.19	2.28(-4)
	21 8 13 0	–	20 8 12 0	260415.333	179.19	2.29(-4)
	20 10 11 1	–	20 9 12 1	260643.800	190.33	2.07(-5)
	20 10 10 2	–	20 9 11 2	260655.151	190.34	2.07(-5)
	20 10 10 0	–	20 9 11 0	260682.101	190.34	2.07(-5)
	20 10 11 0	–	20 9 12 0	260682.850	190.34	2.07(-5)
	19 4 16 0	–	18 3 15 0	260788.406	123.25	1.70(-5)
	19 4 16 1	–	18 3 15 2	260793.540	123.26	1.70(-5)
	11 5 6 5	–	10 4 6 5	260799.899	242.97	1.90(-5)
	32 3 29 2	–	32 2 30 2	260916.838	316.40	1.31(-5)
	32 3 29 0	–	32 2 30 0	261005.113	316.40	1.31(-5)
	32 4 29 0	–	32 3 30 0	261070.724	316.40	1.31(-5)
	19 10 10 1	–	19 9 11 1	261084.120	178.50	2.01(-5)
	19 10 9 2	–	19 9 10 2	261095.680	178.51	2.01(-5)
	19 10 9 0	–	19 9 10 0	261126.435	178.50	2.01(-5)
	19 10 10 0	–	19 9 11 0	261126.726	178.50	2.01(-5)
	21 5 17 1	–	20 5 16 1	261148.904	154.10	2.54(-4)

Table B.6: continued.

Species Database	Transition			Frequency (MHz)	E_{up} (K)	A_{ij} (s^{-1}) $a(b) = a \times 10^b$
	21 5 17 0	–	20 5 16 0	261165.456	154.09	2.54(-4)
	21 6 16 4	–	20 6 15 4	261234.608	347.62	2.43(-4)
	21 7 15 0	–	20 7 14 0	261433.791	169.52	2.41(-4)
	21 7 15 1	–	20 7 14 1	261436.771	169.52	2.36(-4)
	18 10 9 1	–	18 9 10 1	261458.040	167.26	1.94(-5)
	18 10 8 2	–	18 9 9 2	261469.927	167.28	1.94(-5)
	18 10 8 0	–	18 9 9 0	261504.039	167.27	1.94(-5)
	18 10 9 0	–	18 9 10 0	261504.039	167.27	1.94(-5)
	21 7 14 2	–	20 7 13 2	261715.518	169.55	2.37(-4)
	21 6 15 5	–	20 6 14 5	261727.149	348.04	2.45(-4)
CH_2OHCHO (GA), v=0	29 11 18 0	–	29 10 19 0	258059.438	315.77	2.78(-4)
CDMS	29 11 19 0	–	29 10 20 0	258123.981	315.77	2.78(-4)
	22 4 19 0	–	21 3 18 0	258128.769	150.22	2.53(-4)
	40 6 34 0	–	40 5 35 0	259147.668	488.73	2.40(-4)
	28 11 17 0	–	28 10 18 0	259179.986	299.53	2.77(-4)
	28 11 18 0	–	28 10 19 0	259212.684	299.53	2.77(-4)
	27 11 16 0	–	27 10 17 0	260165.716	283.86	2.75(-4)
	27 11 17 0	–	27 10 18 0	260181.761	283.86	2.75(-4)
	40 7 34 0	–	40 6 35 0	260691.347	488.81	2.44(-4)
	26 11 15 0	–	26 10 16 0	261033.098	268.76	2.72(-4)
	26 11 16 0	–	26 10 17 0	261040.709	268.76	2.72(-4)
	24 4 20 0	–	23 5 19 0	261041.952	182.31	1.89(-4)
	24 2 22 0	–	23 3 21 0	261257.959	167.42	3.73(-4)
	24 3 22 0	–	23 2 21 0	261655.476	167.43	3.75(-4)
a-$(CH_2OH)_2$ (*a*-EG)	27 3 25 0	–	26 3 24 1	258184.073	186.63	4.19(-4)
CDMS	27 2 25 0	–	26 2 24 1	258250.590	186.62	4.10(-4)
	27 1 26 0	–	26 2 25 0	258567.278	179.35	7.15(-5)
	27 1 26 1	–	26 2 25 1	258575.594	179.69	7.16(-5)
	27 2 26 0	–	26 1 25 0	258579.070	179.35	7.11(-5)
	27 2 26 1	–	26 1 25 1	258586.940	179.69	7.21(-5)
	26 6 21 0	–	25 6 19 0	259084.460	191.35	3.28(-5)
	26 23 3 0	–	25 23 2 1	259084.899	431.87	9.23(-5)
	26 23 4 0	–	25 23 3 1	259084.899	431.87	9.23(-5)
	26 21 5 0	–	25 21 4 1	259177.002	388.80	1.48(-4)
	26 21 6 0	–	25 21 5 1	259177.002	388.80	1.48(-4)
	27 1 27 1	–	26 1 26 0	259202.265	171.76	4.28(-4)
	27 0 27 1	–	26 0 26 0	259202.322	171.76	4.28(-4)
	11 8 3 0	–	10 7 3 1	259222.484	63.87	1.55(-5)
	11 8 4 0	–	10 7 4 1	259222.486	63.87	1.55(-5)
	26 20 6 0	–	25 20 5 1	259229.051	368.72	1.74(-4)
	26 20 7 0	–	25 20 6 1	259229.051	368.72	1.74(-4)
	26 19 7 0	–	25 19 6 1	259286.996	349.62	1.98(-4)
	26 19 8 0	–	25 19 7 1	259286.996	349.62	1.98(-4)
	26 18 8 0	–	25 18 7 1	259352.696	331.48	2.22(-4)
	26 18 9 0	–	25 18 8 1	259352.696	331.48	2.22(-4)
	26 17 9 0	–	25 17 8 1	259428.525	314.32	2.44(-4)
	26 17 10 0	–	25 17 9 1	259428.525	314.32	2.44(-4)
	26 16 10 0	–	25 16 9 1	259517.576	298.14	2.65(-4)
	26 16 11 0	–	25 16 10 1	259517.576	298.14	2.65(-4)
	26 15 11 0	–	25 15 10 1	259623.977	282.95	2.85(-4)
	26 15 12 0	–	25 15 11 1	259623.977	282.95	2.85(-4)
	26 14 12 0	–	25 14 11 1	259753.385	268.74	3.03(-4)
	26 14 13 0	–	25 14 12 1	259753.385	268.74	3.04(-4)
	25 5 20 0	–	24 5 19 1	259810.009	174.98	4.14(-4)
	26 3 23 0	–	25 4 22 0	259898.267	180.03	1.90(-4)
	26 13 13 0	–	25 13 12 1	259913.769	255.51	3.21(-4)
	26 13 14 0	–	25 13 13 1	259913.769	255.51	3.21(-4)
	26 12 15 0	–	25 12 14 1	260116.738	243.28	3.38(-4)
	26 12 14 0	–	25 12 13 1	260116.738	243.28	3.38(-4)

Table B.6: continued.

Species Database	Transition			Frequency (MHz)	E_{up} (K)	A_{ij} (s^{-1}) $a(b) = a \times 10^b$
	26 11 16 0	–	25 11 15 1	260379.902	232.05	3.53(-4)
	26 11 15 0	–	25 11 14 1	260379.910	232.05	3.53(-4)
	24 4 20 1	–	23 4 19 0	260662.054	159.41	4.03(-4)
	26 10 17 0	–	25 10 16 1	260731.312	221.83	3.68(-4)
	26 10 16 0	–	25 10 15 1	260731.522	221.83	3.68(-4)
	25 4 22 1	–	24 4 21 0	260738.168	167.90	1.45(-4)
	28 2 27 0	–	27 2 26 1	260759.249	192.20	4.32(-4)
	28 1 27 0	–	27 1 26 1	260760.891	192.20	4.31(-4)
	27 4 23 1	–	26 5 22 1	260993.665	198.65	9.51(-5)
	26 5 22 0	–	25 5 21 1	261181.033	185.84	3.79(-4)
	26 9 18 0	–	25 9 17 1	261217.419	212.64	3.82(-4)
	26 9 17 0	–	25 9 16 1	261221.825	212.64	3.82(-4)
	28 0 28 0	–	27 1 27 0	261304.289	183.96	8.62(-5)
	28 1 28 0	–	27 0 27 0	261304.396	183.96	8.62(-5)
	28 0 28 1	–	27 1 27 1	261316.502	184.30	8.64(-5)
	28 1 28 1	–	27 0 27 1	261316.604	184.30	8.64(-5)
g-$(CH_2OH)_2$ (g-EG) CDMS	19 3 16 0	–	18 2 16 1	258132.256	99.64	8.77(-5)
	25 6 20 1	–	24 6 19 0	258140.799	177.14	1.49(-4)
	25 4 22 1	–	24 3 21 1	258146.236	166.51	5.54(-5)
	25 7 18 1	–	24 7 17 0	258193.293	183.22	1.40(-4)
	25 4 22 0	–	24 3 21 0	258228.389	166.46	1.24(-4)
	27 4 23 0	–	26 5 22 0	258328.455	196.89	5.30(-5)
	27 4 23 1	–	26 5 22 1	258376.787	196.94	6.77(-5)
	27 2 26 1	–	26 2 25 0	258670.537	178.47	1.62(-4)
	27 1 26 1	–	26 1 25 0	258673.113	178.47	1.65(-4)
	28 1 28 0	–	27 1 27 1	258855.869	183.15	1.66(-4)
	28 0 28 0	–	27 0 27 1	258855.890	183.15	1.66(-4)
	17 2 16 1	–	16 1 16 0	258880.434	74.76	3.25(-5)
	25 6 19 0	–	24 6 18 1	259076.676	177.52	1.52(-4)
	26 4 23 0	–	25 4 22 1	259858.291	178.98	9.58(-5)
	28 0 28 1	–	27 1 27 1	260191.593	183.21	1.70(-4)
	28 1 28 1	–	27 0 27 1	260191.662	183.21	1.70(-4)
	28 0 28 0	–	27 1 27 0	260193.105	183.15	1.70(-4)
	28 1 28 0	–	27 0 27 0	260193.175	183.15	1.70(-4)
	19 3 16 1	–	18 2 16 0	260466.788	99.70	9.11(-5)
	25 4 21 0	–	24 4 20 1	260784.969	170.44	1.63(-4)
	25 6 19 1	–	24 6 18 0	261211.160	177.57	1.54(-4)
	26 3 23 0	–	25 3 22 1	261231.929	178.81	2.07(-4)
	18 5 14 1	–	17 4 13 1	261293.071	96.03	4.57(-5)
	18 5 14 0	–	17 4 13 0	261378.330	95.98	6.03(-5)
	28 1 28 1	–	27 1 27 0	261528.877	183.21	1.71(-4)
	28 0 28 1	–	27 0 27 0	261528.899	183.21	1.72(-4)
	26 4 23 1	–	25 4 22 0	261644.038	179.02	2.06(-4)